Extracting quantum-critical properties from directly evaluated enhanced perturbative continuous unitary transformations

Master's Thesis in Physics

presented by

Lukas Schamriß

01.12.2023

Institut für Theoretische Physik I
Friedrich-Alexander-Universität Erlangen-Nürnberg

Betreuer:
Matthias Walther
Prof. Dr. Kai Phillip Schmidt

Abstract

Ising models in a transverse field are paradigmatic models for quantum phase transitions of various universality classes depending on the lattice geometry and the choice of antiferromagnetic or ferromagnetic coupling. We investigate the quantum phase diagram of the bilayer antiferromagnetic transverse-field Ising model on the triangular lattice with an Ising-type interlayer coupling. Without a field, the model is known to host a classically disordered ground state, and in the limit of decoupled layers it exhibits the 3d-XY *'order by disorder'* transition of the corresponding single-layer model. Our starting point for the unknown parts of the phase diagram is a high-order perturbative calculation from the limit of isolated dimers where the model is in a gapped phase. Directly evaluated enhanced perturbative continuous unitary transformations (deepCUTs) are used to calculate non-perturbatively extrapolated numerical data for the ground-state energy and the energy gap which coincide with the perturbative series up to the order with respect to which the deepCUT is truncated. We develop a general scheme to extract quantum critical properties from the deepCUT data based on critical scaling and a strict correspondence between the truncation used for deepCUT and the length scale of correlations at the critical point.

Contents

1 Introduction

Already in 1950, Wannier and Houtappel realized that the antiferromagnetic Ising model on the triangular lattice does not order even at zero temperature [1, 2]. Instead, the ground state of the model exhibits a macroscopic degeneracy which is against the naive expectation given by the third law of thermodynamics, since the zero-temperature entropy of the system is extensive and hence depends on the number of particles. This phenomenon is a manifestation of the geometrical frustration present in the model. It has been described by Moessner in the context of Ising models [3] and stems from positive exchange integrals inducing antiferromagnetic couplings in combination with a geometry not allowing for a unique energy-minimizing state. Moessner proposed frustrated Ising models in a transverse field as paradigmatic systems to study the interplay of quantum dynamics with classical frustration. If an infinitesimal transverse field is applied to the macroscopically degenerate ground states, the degeneracy is lifted by the introduced quantum fluctuations. The emergent phases can be of manifold nature. For the triangular lattice a so called *'order by disorder'* scenario takes place with an ordered phase up to a second-order phase transition [4] while on the related Kagome lattice a *'disorder by disorder'* scenario leads to a disordered phase in the whole parameter range [5]. Furthermore, frustration has more generally been shown to be a knob stabilizing unconventional phases of matter such as spin liquids [6], spin ices as in the pyrochlore lattice [7] and even topological phases, most prominently realized by the Kitaev model [8]. An interesting link to quantum dimer models has been pointed out by Moessner [9]. To study the phase diagrams of models with competing interactions such as the earlier mentioned systems, numerical methods capable of capturing strong correlations must be applied. The goal of this thesis is to establish directly evaluated enhanced perturbative continuous unitary transformations (deepCUT) [10] as a tool to characterize second-order quantum phase transitions. In order to demonstrate that our approach is competitive, we construct the frustrated transverse-field Ising bilayer on the triangular lattice which is expected to host an *'order by disorder'* scenario in the single-layer limit. We aim to investigate its entire phase diagram which has not been achieved so far to our knowledge. The construction is inspired by earlier findings which have revealed novel quantum phase transitions in bilayer and multilayer systems such as in the stacked toric code [11, 12].

Investigating quantum criticality with perturbative methods usually involves a non-perturbative extrapolation in order to account for the truncated long-range correlations in the critical regime. A widely applied method is the perturbative continuous unitary transformation (pCUT) [13, 14], which is a method to efficiently calculate high-order series expansions, typically using graph and linked-cluster expansions. The standard approach for the extrapolation are dlog-Padé approximants [15] whose Taylor series is exactly the perturbative series up to the order in which the perturbative result is available. The higher orders in their expansion are designed to capture critical behavior like power laws. Moreover, there exists a variety of methods which are considered non-perturbative but share the property of dlog-Padé approximants that they recover the perturbative series up to a specific order and add extrapolated higher orders. First of all there is the numerical linked-cluster expansion (NLCE) which exploits exact diagonalization in combination with a linked-cluster expansion for the extrapolation. The recently introduced projective cluster-additive transformation (PCAT) allows to extend the range of applicability from ground states to excitations [16]. Both is as well achieved by the graph-theory based continuous unitary transformation (gCUT) [17] which however also is known to have problems with convergence [18], as well as NLCE using PCAT. In the context of gCUT, a general approach to extract quantum criticality from non-perturbative numerical data based on dlog-Padé extrapolations has been introduced [19]. Further methods based on flow equations which is the continuous similarity transformation (CST) for gapless phases [20, 21] and the self-similar continuous unitary transformation (sCUT) [22]. CST operates in the momentum space and applies a truncation in the scaling dimension which is tuned to capturing critical properties. It has been applied successfully to a transition in the easy-axis antiferromagnetic XXZ model, but no general way of analysis for quantum criticality has been established. The analysis of results from sCUTs have been found to be intricate since the truncation in real space must be designed manually which limits the control over the truncation errors. DeepCUT shares the property to be a non-perturbative method capturing a perturbative series. If explicitly only the series is calculated in the framework, the transformation is called enhanced perturbative continuous unitary transformation (epCUT) and is a direct extension of pCUT since it cures the limitation of pCUT to equidistant spectra in the unperturbed Hamiltonian. However, the flow equation in that generalized case must be solved numerically and the linked cluster property of the transformation has so far not been used for a linked-cluster expansion, in contrast to pCUT. This makes the method significantly more expensive computationally such that the accessible perturbative orders are lower than for pCUT, NLCE or PCAT. Recently, pcst^{++} has been introduced [23] as a new method which also avoids the restriction of pCUT to equidistant spectra. In contrast to epCUT, the flow equation is still solved algebraically as for pCUT and as an additional feature, pcst^{++} can also be used to treat open systems. The strength of epCUT lies in its non-perturbative extrapolation achieved by deepCUT. The algorithmic requirements and the computational cost are almost the same as for epCUT, it has been shown to be a quantitatively robust extrapolation as compared to dlog-Padé extrapolations [10] and solves the issue of the truncation not being well-defined for sCUTs. DeepCUT has widely been applied [24–26] to investigate properties of models in parameter regimes where the perturbative series is not meaningful anymore. In most cases one-dimensional models are considered and to our knowledge no efforts have been made to access universal properties of quantum phase transitions. We only are aware of one application of deepCUT to a two-dimensional model [27] which neither has addressed quantum criticality. In the project of this thesis, we want to fill this gap and investigate for multiple two-dimensional models, how the universality classes which the models fall into can be discriminated with deepCUT.

The thesis is organized as follows. In Chapter 2, the theoretical basis for the analysis is given. This includes a discussion of quantum criticality in general and specifically the scaling behavior of the ground-state energy and the energy gap. Moreover, the models we treat with deepCUT and, in particular, the frustrated transverse-field Ising bilayer on the triangular lattice are introduced. In Chapter 3, the concept of flow equations and the truncation of deepCUT are reviewed, followed by an explanation of the algorithmic implementation for this project. In the first part of Chapter 4, the numerical results for various single-layer TFIMs are shown and used to establish a robust and controlled way of extracting critical exponents and the critical point from deepCUT data of the energy gap and the ground-state energy. In the second part of that chapter, the scheme is successfully applied to the frustrated transverse-field Ising bilayer. The findings of this thesis are summarized in Chapter 5 and an outlook is given.

2 Quantum criticality of transverse-field Ising models

2.1 Quantum phase transitions

We consider a Hamiltonian for a lattice model $H = H_0 + gH_1$ which depends on a dimensionless parameter g. A quantum phase transition occurs if the the ground-state energy $E_0(g)$ shows non-analytic behavior with respect to g at a critical value g_{c}. Quantum phase transitions are closely related to classical phase transitions in thermodynamic models with the ground-state energy taking over the role of the thermodynamic potential. Therefore, they can as well be divided into first and second-order phase transitions. First-order quantum phase transitions exhibit a discontinuity in the first derivative of the ground-state energy, while second-order phase transitions typically show the non-analyticity in the second derivatives of the ground-state energy such as the heat capacity or the magnetic susceptibility. The latter second-order transitions follow the same universality classes as classical phase transitions. This can be understood in the context of quantum-classical mappings [28] which link d-dimensional quantum models at temperature $T = 0$ to $(d+1)$-dimensional classical models at $T > 0$. The mechanism allowing for these mappings is a correspondence between thermal fluctuations and quantum fluctuations. Even though $T = 0$ is not physically realizable, traces of a quantum critical point can be observed at low temperatures. This is illustrated in Fig. 2.1. Above the critical point lies a quantum critical region where thermal and quantum fluctuations are comparably important. This influences the dynamics of the system also at finite temperature.

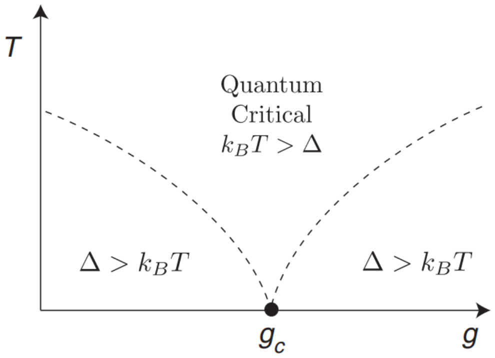

Figure 2.1: Schematic of a quantum phase transition at low temperatures. At zero temperature the control parameter g tunes the system from one phase to the other at the quantum critical point g_c. At finite temperature, a quantum critical region is found instead. Figure taken from [28].

In this thesis, we only consider second-order quantum phase transitions. In the vicinity of a second-order phase transition, the length scale of the quantum fluctuations diverges and the properties of the system are usually described by universal power laws which are determined by the universality class of the transition. The behavior of the correlation length ξ is described by a power law with the universal critical exponent ν:

$$\xi \sim |g - g_c|^{-\nu} . \tag{2.1}$$

The second derivative of the ground-state energy with respect to the control parameter corresponds to the classical specific heat C and therefore follows a power law according to the critical exponent α:

$$C \sim \partial_g^2 E_0 \sim |g - g_c|^{-\alpha} . \tag{2.2}$$

Furthermore, the correlation time τ of the quantum fluctuations is related to the correlation length by the dynamical critical exponent z

$$\tau \sim \xi^z \tag{2.3}$$

which allows for expressing the scaling of the energy gap Δ as

$$\Delta \sim |g - g_c|^{z\nu} . \tag{2.4}$$

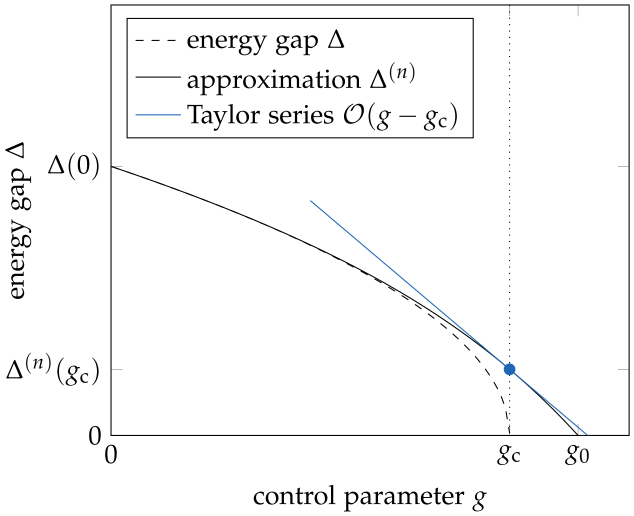

Figure 2.2: Illustration of the derivation for the scaling relation for the closing of the gap. The exact gap is approximated by data $\Delta^{(n)}$. The closing of the approximation at g_0 is further approximated by a first-order Taylor series at the critical point. This approximation is analytically accessible if it is considered as the inverse function mapping gap values Δ to control parameter values g. Considering the n-th-order Taylor series, the scaling of $\xi^{-\frac{1}{\nu}}$ for the closing of the gap can be derived.

In order to link the introduced scaling properties to the perturbative methods such as NLCE or deepCUT, the correspondence between truncation and length scale must be understood. In the context of flow equations, the truncation of deepCUT for a fixed basis is minimal under the condition, that the results are correct up to a given order n in a perturbative parameter. In order to examine quantum phase transitions we choose this parameter to be g. A property of perturbation theory in lattice systems with short-range interactions is that the spatial extent of the relevant quantum fluctuations increases with the perturbative order n. This is expected to be reflected in the length scale of the correlations ξ. The exact relation between ξ and n depends on the method, however. For NLCE, the relation

$$\xi \propto n_{\text{NLCE}}^{\frac{1}{2}} \tag{2.5}$$

is typically found if the number of bonds is considered as the perturbative order [16, 18] which is also confirmed later in this thesis. For deepCUT we find the correspondence

$$\xi \propto n_{\mathrm{deepCUT}}, \tag{2.6}$$

instead. Therefore, we are interested in the dependence of critical quantities on the length scale. For the heat power law of the capacity C we derive from Eqs. 2.1 and 2.2

$$C \sim \xi^{\frac{\alpha}{\nu}}. \tag{2.7}$$

For the energy gap we can directly derive the relation from Eqs. 2.1 and 2.4:

$$\Delta \sim \xi^{-z}. \tag{2.8}$$

When studying quantum phase transitions, the numerical determination of critical exponents is the key to classifying the universality and by doing so, achieving physical understanding in the non-trivial parameter regime of competing interactions. That the energy gap does not directly give access to the critical exponent ν if it is only available as a function of ξ as in Eq. 2.8, is undesirable since space-time isotropy encoded by $z = 1$ holds in a wide range of models no matter of which universality class they fall into [28]. Instead, for discriminating universality classes, ν can be determined based on the first derivative of the gap, which has also been pointed out by Hamer [29]:

$$\partial_g \Delta \sim |g - g_{\mathrm{c}}|^{z\nu - 1} \sim \xi^{-z+\frac{1}{\nu}}. \tag{2.9}$$

For the n-th derivative one finds

$$\partial_g^n \Delta \sim |g - g_{\mathrm{c}}|^{z\nu - n} \sim \xi^{-z+\frac{n}{\nu}} \tag{2.10}$$

where $z\nu \notin \mathbb{N}$ is assumed.

Furthermore, the closing of the gap is a meaningful quantity which gives access to the critical point. It is crucial to realize that the energy gap at a finite length scale is not expected to close at the critical point, however. One can either consider a gap value close to, but not at the critical point to capture a finite correlation length or an approximation of the gap characterized by finite correlation length such as obtained from deepCUT, NLCE or finite system sizes in general. For such data no non-analyticity is expected at the critical point. To highlight this, $\Delta^{(n)}$ is used to denote a finite-order or finite-length-scale approximation of the gap. Under the assumption that

$\Delta^{(n)}$ is analytic at the critical point g_c, the power law for the gap and its derivatives can be inserted into a Taylor expansion around g_c:

$$\Delta^{(n)}(g) = \sum_{n=0}^{\infty} \frac{\partial_g^n \Delta^{(n)}(g_c)}{n!} (g - g_c)^n. \tag{2.11}$$

The goal of expanding the approximate gap is to find a power law for the closing of the gap g_0 at finite correlation length. The idea behind this expansion is illustrated in Fig. 2.2. The label $\Delta^{(n)}$ for the approximation is reduced to Δ in the following. The expansion can be used to recursively find the inverse function $g(\Delta^{(n)})$ as a Taylor expansion around the gap value $\Delta^{(n)}(g_c)$

$$\begin{aligned} g(\Delta^{(n)}) = g_c + \frac{1}{\partial_g \Delta^{(n)}(g_c)} (\Delta^{(n)} - \Delta^{(n)}(g_c)) \\ - \frac{\partial_g^2 \Delta^{(n)}(g_c)}{2(\partial_g \Delta^{(n)}(g_c))^3} (\Delta^{(n)} - \Delta^{(n)}(g_c))^2 + \dots \end{aligned} \tag{2.12}$$

which up to second order in $\Delta^{(n)}$ yields the scaling behavior of the closing of the gap, considering the scaling behavior of the derivatives $\partial_g^n \Delta^{(n)}$ given in Eq. 2.10 and $\Delta^{(n)} - \Delta^{(n)}(g_c) \sim \xi^{-z}$. By setting $\Delta^{(n)} = 0$ and using $g(\Delta^{(n)} = 0) = g_0$ we find the relation

$$g_0 - g_c \sim \xi^{-\frac{1}{\nu}} \tag{2.13}$$

with respect to perturbative order n for first and second order in $\Delta^{(n)}$.

It can further be checked that this holds for any finite order. We introduce the variables

$$\gamma := g - g_c, \; \delta := \Delta^{(n)} - \Delta^{(n)}(g_c) \tag{2.14}$$

such that we can express Δ as $\delta(\gamma)$ with $\delta(0) = 0$. This shifts the system of coordinates to the critical point and the approximate value of the gap at the critical point. To the resulting functions we can apply Lagranges inversion theorem in its form for a power series, stating

$$\delta^{-1}(x) = \sum_{n=1}^{\infty} \frac{x^n}{n} \left[\gamma^{n-1}\right] \left(\frac{\gamma}{\delta(\gamma)}\right)^n \tag{2.15}$$

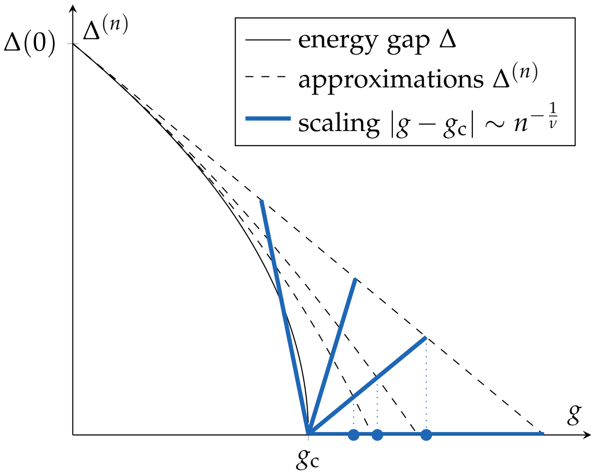

Figure 2.3: Illustration of the general result for the scaling of $|g-g_{\mathrm{c}}|$. Given data $\Delta^{(n)}(g)$ which approximates the energy gap with respect to a specific length scale given by n. The g-values at which $\Delta^{(n)}$ takes the value $\epsilon\Delta^{(n)}(g_{\mathrm{c}})$ approach g_{c} with the exponent $\frac{1}{\nu}$ for any ϵ. For $\epsilon = 0$ one finds the relation for the closing of the gap. Note that the other blue lines indicating scaling, are not expected to be linear as shown in the illustration.

with $[x^n]f(x)$ denoting the coefficient of x^n in the expansion of f around 0. This is the general form for the series in Eq. 2.12. The gap closes at g_0 which can be expressed as $g_{\mathrm{c}} + \delta^{-1}(-\Delta(g_{\mathrm{c}}))$. For $g_0 - g_{\mathrm{c}}$ we find the scaling behavior

$$\begin{aligned}
\delta^{-1}(-\Delta^{(n)}(g_{\mathrm{c}})) &= \sum_{n=1}^{\infty} \frac{(-\Delta^{(n)}(g_{\mathrm{c}}))^n}{n} \left[\gamma^{n-1}\right] \left(\frac{\gamma}{\delta(\gamma)}\right)^n \\
&\sim \sum_{n=1}^{\infty} \gamma^{z\nu n} \left[\gamma^{n-1}\right] \left(\frac{\gamma}{\gamma^{z\nu}}\right)^n \\
&\sim \sum_{n=1}^{\infty} \gamma^{z\nu n} \gamma^{-n+1} \gamma^{n-z\nu n} \\
&\sim \gamma \sim \xi^{-\frac{1}{\nu}}
\end{aligned} \tag{2.16}$$

for every order individually in accordance to the earlier finding up to second order.

The last derivation can as well be carried out by setting $\Delta^{(n)} = \epsilon\Delta^{(n)}(g_{\mathrm{c}})$ for

δ instead of $\Delta = 0$. This implies that also $\delta^{-1}(\Delta^{(n)}(g_c))$ scales proportional to $\xi^{-\frac{1}{\nu}}$ as the closing of the gap. Intuitively, this is the distance of the g-value where the gap takes the ϵ-fold value of the critical point:

$$g_{(\Delta^{(n)}=\epsilon\Delta^{(n)}(g_c))} - g_c \sim \xi^{-\frac{1}{\nu}}. \tag{2.17}$$

This implies a family of series $\{g_n\}_n$ which all scale in the same way. This is illustrated in Fig. 2.3. The derivation of this result relies on the considered approximation to be analytic in the sense that the Taylor series shown in Fig. 2.2 converges quickly. The requirement is that the scaling relation derived for the n-th derivative of the energy gap holds for all relevant orders n up to sufficient accuracy. This is practically not to be expected for arbitrary high orders. In a broader context the result is remarkable since it derives the scaling form

$$\Delta(g - g_c) = \xi^{-z}\Delta(\xi^{\frac{1}{\nu}}(g - g_c)) \tag{2.18}$$

from the relations for the derivatives of the gap in Eq. 2.10. This scaling form for the energy gap has been considered by Hamer [29]. Our derivation of the result is straight forwardly extended to other quantities such as the magnetization or the heat capacity.

2.2 Transverse-field Ising models

Ising models are paradigmatic models for phase transitions. We begin by introducing the Hamiltonian of a general transverse-field Ising model (TFIM) with nearest-neighbor interaction. A spin-$\frac{1}{2}$ degree of freedom on site i is represented by standard Pauli matrices $\sigma_i^{x,y,z}$. The Hamiltonian reads

$$H_I = J \sum_{\langle i,j \rangle} \sigma_i^x \sigma_j^x + h \sum_i \sigma_i^z \tag{2.19}$$

where J is the coupling constant of the interaction and h the field strength of an externally applied magnetic field orthogonal to the direction along which the spins interact. The Hamiltonian can be rewritten in second quantization in terms of hardcore bosons with creation and annihilation operators $b_i^\dagger, b_i$ and the commutation relation

$$\left[b_i, b_j^\dagger\right] = \delta_{ij}\left(1 - 2n_i\right). \tag{2.20}$$

The operator n_i with eigenvalues $0, 1$ counts the number of quasi-particles at site i and is defined as $b_i^\dagger b_i$. Up to a constant shift in the energy the Hamiltonian in terms of hardcore bosons reads

$$H_I = 2h\sum_i n_i + J\sum_{\langle i,j\rangle}\left(b_i^\dagger + b_i\right)\left(b_j^\dagger + b_j\right). \tag{2.21}$$

TFIMs can host a variety of phases and quantum phase transitions which make them an interesting object of investigation. In this thesis we consider the square and triangular lattice in two dimensions with ferromagnetic ($J < 0$) and antiferromagnetic ($J > 0$) coupling. For all these cases the respective quantum phase diagram has been explored numerically and can be used to benchmark the performance of deepCUT close to critical points. Furthermore, we introduce the frustrated transverse-field Ising bilayer on the triangular lattice for which the phase diagram has not been explored to our knowledge.

2.3 Models in the (2+1)d Ising universality class

All discussed models have the same ground state in the high-field (HF) limit $h \gg J$

$$\psi_0^{\mathrm{HF}} = |\uparrow\uparrow\ldots\rangle =: |\Uparrow\rangle\,, \tag{2.22}$$

to which a polarized phase is connected adiabatically throughout. The phase adiabatically connected to the low-field (LF) limit depends on the coupling and the lattice geometry. For ferromagnetic coupling the ground state in the LF limit can be written in terms of eigenstates of the Pauli x-matrix $|\rightarrow\rangle, |\leftarrow\rangle$ as an arbitrary superposition

$$\psi_0^{\mathrm{LF}} = a\,|\rightarrow\rightarrow\ldots\rangle + b\,|\leftarrow\leftarrow\ldots\rangle = a\,|\Rightarrow\rangle + b\,|\Leftarrow\rangle\,. \tag{2.23}$$

Since the square lattice is bipartite, the corresponding TFIM has the same phase diagram for ferro- and antiferromagnetic coupling. Therefore these

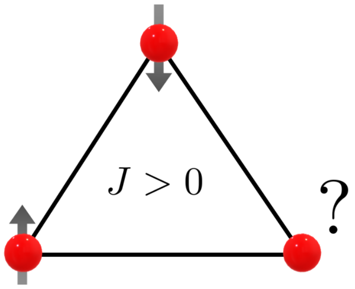

Figure 2.4: Illustration of the origin of geometrical frustration. Antiferromagnetic couplings on a triangle cannot be satisfied simultaneously.

three models belong to the 3d Ising universality class. Only in the antiferromagnetic TFIM on the triangular lattice the second phase is fundamentally different and will be discussed separately.

2.4 The 3dXY transition in the antiferromagnetic TFIM on the triangular lattice

The antiferromagnetic TFIM on the triangular lattice is distinct from others since it is geometrically frustrated. The phenomenon is illustrated in Fig. 2.4. Within any plaquette in the triangular lattice there is no configuration minimizing the interaction energy at all three bonds individually. Only two bonds can be satisfied simultaneously and any global configuration which satisfies that constraint on all plaquettes is part of the ground state manifold in the LF limit. Hence, the ground state in the limiting case is extensively degenerate. However, the transverse magnetic field induces fluctuations consisting of local spin flips. Hence, the onset of the field mixes the degenerate ground states and splits the degenerate energy level into many distinct levels. The energy gain or loss for each configuration is determined by how flippable it is. The ground-state manifold for fields $h > 0$ consists only of three configurations [3] and hence, is only intensively

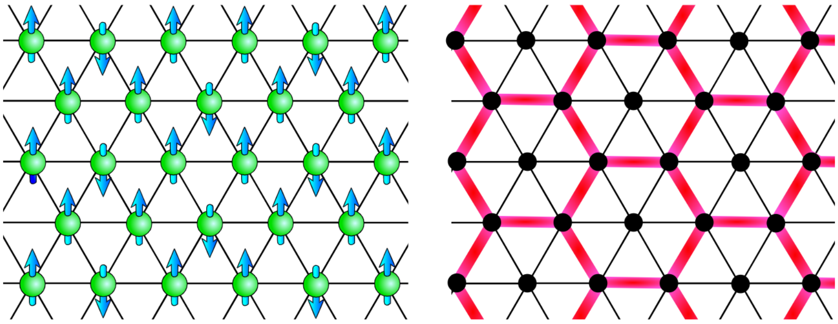

Figure 2.5: Illustrations of the most flippable spin state in the clock-ordered phase of the frustrated TFIM on the triangular lattice. The spins are aligned according to a hexagonal structure resulting in a three times enlarged unit cell. This structure allows for the highest energy gain from the fluctuations introduced by a transverse field. Figure taken from [5].

degenerate. This ordering process induced by the magnetic field is also referred to as *'order by disorder'*. The ground states are illustrated in Fig. 2.5. The nature of the elementary excitation driving the 3dXY transition in the ordered phase could be either another less flippable state in the degenerate ground-state manifold or a state with higher energy also for $h = 0$.

2.5 Frustrated transverse-field Ising bilayer

Based on the TFIMs introduced in the last section, we construct a model which has not yet been investigated in the literature to our knowledge. We obtain the transverse-field Ising bilayer by stacking two TFIMs on the triangular lattice and adding an Ising interaction in x-direction between spins on corresponding sites of the two lattices. Here, a spin on site μ and layer i is represented by $\sigma^{x,y,z}_{\mu i}$. The couplings are illustrated in Fig. 2.6 and the model is described by the Hamiltonian

$$H = J_{\parallel} \sum_{i=1,2} \sum_{\langle \mu,\nu \rangle} \sigma^x_{\mu i} \sigma^x_{\nu i} - J_{\perp} \sum_{\mu} \sigma^x_{\mu 1} \sigma^x_{\mu 2} + \sum_{\mu,i} h_i \sigma^z_{\mu i} \,. \tag{2.24}$$

$J_{\parallel} > 0$ is the interaction strength of the intra-layer coupling inducing geometric frustration while $J_{\perp} > 0$ is the inter-layer coupling. The sign of

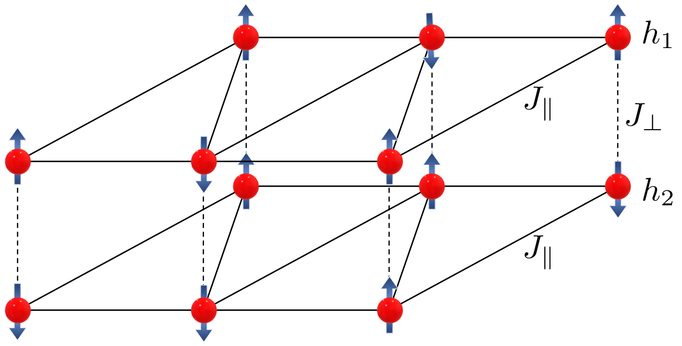

Figure 2.6: Illustration of the frustrated transverse-field Ising bilayer. Two TFIMs with intralayer coupling $J_{||}$ and fields h_i are stacked and coupled via the interlayer coupling $J_\perp$.

$J_\perp$ can be fixed without loss of generality since it can be absorbed into the relative orientation of the spins in layer 1 and 2. The field strengths coupling to the spins in layer 1 and 2 denoted by $h_{1,2}$. For the case $h_1 = h_2$ the model is symmetric under the permutation of the layers.

In the limiting case of vanishing inter-layer coupling, $J_\perp = 0$, the model hosts two copies of the frustrated TFIM on the triangular lattice and hence, the phase diagram contains a quantum critical point of the 3dXY universality class. The phases on either side of the critical point are gapped and hence are expected to extend into the region of non-vanishing inter-layer coupling in the phase diagram. Another boundary of the phase diagram is the case of vanishing field, $h_{1,2} = 0$. Here, the model inherits the extensive ground-state degeneracy from the single-layer TFIM for any ratio of $J_{||}$ and $J_\perp$ since intra- and inter-layer coupling commute. Hence, the ground-state manifold in the limiting case consists of twofold copies of all states in the single-layer manifold. As the perturbation from an infinitesimal field acts by creating local spin flips, the phase for small fields is given by the most flippable spin states which can be identified as the three states known from the single-layer case. The third boundary is the line of decoupled dimers ($J_{||} = 0$). The ground state on this line is unique as long as the field term does not vanish and the state is adiabatically connected to the polarized state in the high-field limit of the decoupled layers. Hence, in the corner of the phase

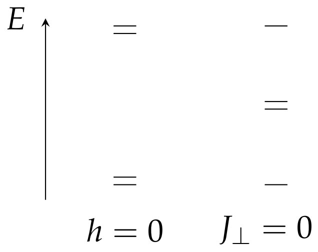

Figure 2.7: Qualitative spectrum of the Hamiltonian $H = J_\perp \sigma_1^x \sigma_2^x + h \sum_i \sigma_i^z$ of a symmetric dimer. On the right-hand side as well as for all intermediate cases one finds an unique ground state. On the left-hand side the ground state is twofold degenerate.

diagram with intra-layer coupling only ($J_\| = h_{1,2} = 0$) must be a transition between the polarized and the ordered phase. The transition in this corner can be understood in the context of a perturbative model in the low-energy physics of the dimers $\sigma_{\mu 1}^x \sigma_{\mu 2}^x$ which will be demonstrated in the Section 2.5.1. Furthermore, two equivalent models which are suited for a series expansion in orders of $J_\|$ starting from decoupled dimers will be introduced in Section 2.5.2.

2.5.1 Low-energy physics in the low-field dimer limit

To describe the low-energy physics in the limit of isolated dimers and low external field, we map the spin degrees of freedom onto a hardcore boson $b_\mu, b_\mu^\dagger$ per site, accounting for the high-energy scale, and a pseudo spin $\tau_\mu^{x,y,z}$ for the low-energy scale as indicated on the left-hand side in Fig. 2.7. Formally, this mapping is given by:

$$\begin{aligned} \sigma_{\mu 1}^z &= \tau_\mu^x (b_\mu^\dagger + b_\mu) & \sigma_{\mu 1}^x &= \tau_\mu^z \\ \sigma_{\mu 2}^z &= b_\mu^\dagger + b_\mu & \sigma_{\mu 2}^x &= \tau_\mu^z (1 - 2 b_\mu^\dagger b_\mu)\,. \end{aligned} \tag{2.25}$$

One can check that indeed the particle number operator $n_\mu = b_\mu^\dagger b_\mu$ encodes the energy of the dimer $\sigma_{\mu 1}^x \sigma_{\mu 2}^x = 1 - 2 n_\mu$. In the low-field limit the energy scale of this interaction is dominant and the low-energy physics driving the phase transition lies within the zero-hardcore-boson sector of the Hilbert space which is described by the pseudo spins. We rewrite the Hamiltonian

$$H = 2J_\perp \sum_\mu n_\mu + J_\| \sum_{\langle\mu\nu\rangle} \tau^z_\mu \tau^z_\nu \Big(1 + (1-2n_\mu)(1-2n_\nu)\Big) + \sum_\mu (h_1\tau^x_\mu + h_2)(b^\dagger_\mu + b_\mu) \quad (2.26)$$

in terms of hardcore bosons and pseudo spins and evaluate an effective Hamiltonian $H_0^{(3)}$ in third-order perturbation theory in $h_{1,2}$ and $J_\|$ under the condition $n_\mu = 0$:

$$H_0^{(3)} = -N\frac{h_1^2+h_2^2}{2J_\perp} + \underbrace{\left(2J_\| - \frac{3}{2}\frac{(h_1^2+h_2^2)J_\|}{J_\perp^2}\right)}_{\widetilde{J}} \sum_{\langle\mu\nu\rangle} \tau^z_\mu\tau^z_\nu - \underbrace{\frac{h_1h_2}{J_\perp}}_{\widetilde{h}} \sum_\mu \tau^x_\mu \,. \quad (2.27)$$

It describes the physics within the low-energy degrees of freedom introduced by an infinitesimal field and corresponds to a single-layer TFIM on the triangular lattice. This implies that in the corner $J_\perp \gg h_{1,2}, J_\|$ of the phase diagram a critical line starts, which divides a polarized and an ordered phase by a 3dXY transition. Given the literature value $x_c := J_c/h = 0.610(4)$ for the single-layer model [30] we can express the onset of the critical line in the phase diagram as

$$x_c \overset{!}{=} \frac{\widetilde{J}}{\widetilde{h}} = 2\frac{J_\|J_\perp}{h_1h_2} - \frac{3}{2}\frac{(h_1^2+h_2^2)J_\|}{h_1h_2J_\perp}. \quad (2.28)$$

By resolving for $J_{\|,c}(h)$ one finds

$$J_{\|,c} = x_c\left(\frac{h_1h_2}{2J_\perp} + \frac{3(h_1^2+h_2^2)h_1h_2}{8J_\perp^3}\right) + \mathcal{O}(h^4) \quad (2.29)$$

where the cubic order exactly vanishes. Hence, the given fourth order in h is not exact but a correction stemming from the third-order effective couplings. It will be later used to estimate the convergence of the expansion of the critical line.

2.5.2 The dimer limit as a starting point for series expansions

In this section, two models will be derived which express the bilayer TFIM as a single layer model with three instead of one excitation per site. This can be achieved by defining quasi-particles as eigenstates of the dimers. The Hamiltonian of a local dimer reads

$$H_{\text{dimer}} = J_\perp \sigma_1^x \sigma_2^x + \sum_i h_i \sigma_i^z . \tag{2.30}$$

In order to diagonalize it, the spin-flip symmetry induced by the conserved quantity $\sigma_1^z \sigma_2^z$ can be used. A basis respecting that symmetry is given by

$$\begin{pmatrix} |{\rightarrow}{\rightarrow}\rangle + |{\leftarrow}{\leftarrow}\rangle \\ |{\rightarrow}{\rightarrow}\rangle - |{\leftarrow}{\leftarrow}\rangle \\ |{\rightarrow}{\leftarrow}\rangle - |{\leftarrow}{\rightarrow}\rangle \\ |{\rightarrow}{\leftarrow}\rangle + |{\leftarrow}{\rightarrow}\rangle \end{pmatrix} \tag{2.31}$$

in terms of the eigenstates of the Pauli x-operators, $\sigma^x |{\rightarrow}\rangle = |{\rightarrow}\rangle$ and $\sigma^x |{\leftarrow}\rangle = -|{\leftarrow}\rangle$. Introducing the symmetric and antisymmetric combination of the fields $h_\pm := h_2 \pm h_1$ the Hamiltonian in that basis reads

$$H_{\text{dimer}} = \begin{pmatrix} -J_\perp & 0 & 0 & h_+ \\ 0 & -J_\perp & h_- & 0 \\ 0 & h_- & J_\perp & 0 \\ h_+ & 0 & 0 & J_\perp \end{pmatrix} . \tag{2.32}$$

It decouples into two 2×2 subblocks which can be easily diagonalized using the following symbols:

$$\begin{aligned} &\epsilon_\pm = \sqrt{J_\perp^2 + h_\pm^2} \qquad u_\pm = \sqrt{\frac{1}{2}\left(1 - \frac{J_\perp}{\epsilon_\pm}\right)},\ v_\pm = \sqrt{\frac{1}{2}\left(1 + \frac{J_\perp}{\epsilon_\pm}\right)} \\ &\Gamma_\pm = v_+ v_- \pm u_+ u_- \quad \Xi_\pm = -(v_+ u_- \pm u_+ v_-) . \end{aligned} \tag{2.33}$$

With the transformation matrix from the basis in Eq. 2.31 to the eigenbasis

$$S = \begin{pmatrix} v_+ & 0 & 0 & -u_+ \\ 0 & v_- & -u_- & 0 \\ 0 & u_- & v_- & 0 \\ u_+ & 0 & 0 & v_+ \end{pmatrix} \tag{2.34}$$

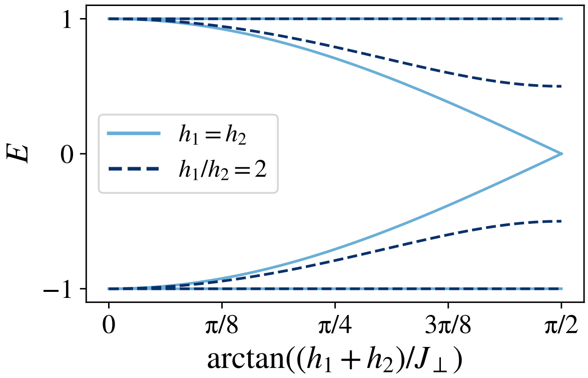

Figure 2.8: Energy spectrum of a local dimer in the frustrated transverse-field Ising bilayer for different ratios of the upper and lower field.

the Hamiltonian transforms to

$$S^{-1} H_{\text{dimer}} S = \begin{pmatrix} -\epsilon_+ & & & \\ & -\epsilon_- & & \\ & & \epsilon_- & \\ & & & \epsilon_+ \end{pmatrix} . \tag{2.35}$$

In Fig. 2.8, the eigenenergies are plotted against the ratio $h_+ / J_\perp \in [0, \infty)$ in units of ϵ_+. In order to derive a model in the eigenbasis, the operators $\sigma^x_{1,2}$ must be transformed. First, in the basis 2.31 the operators read

$$\begin{aligned} \tilde{\sigma}^x_1 &= \begin{pmatrix} 0 & 1 & & \\ 1 & 0 & & \\ & & 0 & 1 \\ & & 1 & 0 \end{pmatrix} , \\ \tilde{\sigma}^x_2 &= \begin{pmatrix} 0 & 1 & & \\ 1 & 0 & & \\ & & 0 & -1 \\ & & -1 & 0 \end{pmatrix} . \end{aligned} \tag{2.36}$$

By applying the transformation matrix S we find the operators in the sought eigenbasis:

$$S^{-1}\tilde{\sigma}_1^x S = \begin{pmatrix} 0 & \Gamma_+ & \Xi_- & 0 \\ \Gamma_+ & 0 & 0 & -\Xi_- \\ \Xi_- & 0 & 0 & \Gamma_+ \\ 0 & -\Xi_- & \Gamma_+ & 0 \end{pmatrix}, \tag{2.37}$$

$$S^{-1}\tilde{\sigma}_2^x S = \begin{pmatrix} 0 & \Gamma_- & \Xi_+ & 0 \\ \Gamma_- & 0 & 0 & \Xi_+ \\ \Xi_+ & 0 & 0 & -\Gamma_- \\ 0 & \Xi_+ & -\Gamma_- & 0 \end{pmatrix}. \tag{2.38}$$

Looking at Fig. 2.8, it is apparent that whenever the fields $h_{1,2}$ do not vanish, a unique ground state in each dimer can be identified. The product of these states serves as the vacuum state in the quasi-particle description. The three remaining states per dimer are local excitations and can be expressed either by two independent quasi-particle flavors with hardcore-bosonic commutation relations, which will be introduced later, or by triplet quasi-particles $t_{1,2,3}$. For this sake we set the vacuum energy to zero and introduce the excitation energies

$$\epsilon_1 := \epsilon_+ - \epsilon_-, \tag{2.39}$$

$$\epsilon_2 := \epsilon_+ + \epsilon_-, \tag{2.40}$$

$$\epsilon_3 := 2\epsilon_+. \tag{2.41}$$

The Hamiltonian in terms of triplet operators

Triplet creation and annihilation operators follow an algebra given by the commutation relations

$$[t_{a\mu}, t^\dagger_{b\nu}] = \delta_{\mu\nu}\left(\delta_{ab} - t^\dagger_{b\mu}t_{a\mu} - \sum_{c=1,2,3} n_{c\mu}\right) \tag{2.42}$$

where indices μ, ν label sites on a lattice. It ensures that on the same site also particles of different flavors follow the hardcore constraint that no more than one particle can exist at a time. In the dimer eigenbasis, the creation operators act on the vacuum $|0\rangle$ as

$$t_1^\dagger\,|0\rangle = \begin{pmatrix}0\\1\\0\\0\end{pmatrix}, \quad t_2^\dagger\,|0\rangle = \begin{pmatrix}0\\0\\1\\0\end{pmatrix}, \quad t_3^\dagger\,|0\rangle = \begin{pmatrix}0\\0\\0\\1\end{pmatrix}. \tag{2.43}$$

The terms of the intra-layer interaction $\sigma^x_{\mu 1}\sigma^x_{\nu 1} + \sigma^x_{\mu 2}\sigma^x_{\nu 2}$ can now be rewritten in triplet creation an annihilation operators. One finds the Hamiltonian

$$\begin{aligned} H = & \sum_{\nu} \sum_{a=1}^{3} \epsilon_a t^\dagger_{a\nu} t_{a\nu} \\ & + J_\parallel \sum_{\langle \mu,\nu \rangle} \Big\{ \Big[\Gamma_+ (t^\dagger_{1\nu} + t^\dagger_{3\nu} t_{2\nu}) + \Xi_- (t^\dagger_{2\nu} - t^\dagger_{3\nu} t_{1\nu}) + \text{h.c.} \Big] \cdot \Big[\nu \to \mu \Big] \\ & \qquad + \Big[\Gamma_- (t^\dagger_{1\nu} - t^\dagger_{3\nu} t_{2\nu}) + \Xi_+ (t^\dagger_{2\nu} + t^\dagger_{3\nu} t_{1\nu}) + \text{h.c.} \Big] \cdot \Big[\nu \to \mu \Big] \Big\} \end{aligned} \tag{2.44}$$

which takes the following form in terms of fundamental processes:

$$\begin{aligned} H = & \sum_{\nu} \sum_{a=1}^{3} \epsilon_a t^\dagger_{a\nu} t_{a\nu} \\ & + J_\parallel \sum_{\langle \mu,\nu \rangle} \Big\{ (\Gamma_+^2 + \Gamma_-^2) \Big[t^\dagger_{1\mu} (t^\dagger_{1\nu} + t_{1\nu}) + \text{h.c.} \Big] \\ & + (\Xi_+^2 + \Xi_-^2) \Big[t^\dagger_{2\mu} (t^\dagger_{2\nu} + t_{2\nu}) + \text{h.c.} \Big] \\ & + (\Gamma_+ \Xi_- + \Gamma_- \Xi_+) \Big[\big(t^\dagger_{1\mu} (t^\dagger_{2\nu} + t_{2\nu}) + (\mu \leftrightarrow \nu) \big) + \text{h.c.} \Big] \\ & + (\Gamma_+^2 - \Gamma_-^2) \Big[\big(t^\dagger_{3\mu} t_{2\mu} (t^\dagger_{1\nu} + t_{1\nu}) + (\mu \leftrightarrow \nu) \big) + \text{h.c.} \Big] \\ & + (\Xi_+^2 - \Xi_-^2) \Big[\big(t^\dagger_{3\mu} t_{1\mu} (t^\dagger_{2\nu} + t_{2\nu}) + (\mu \leftrightarrow \nu) \big) + \text{h.c.} \Big] \\ & + (\Gamma_- \Xi_+ - \Gamma_+ \Xi_-) \Big[\big(t^\dagger_{3\mu} t_{1\mu} (t^\dagger_{1\nu} + t_{1\nu}) + (\mu \leftrightarrow \nu) \big) + \text{h.c.} \Big] \\ & + (\Gamma_+ \Xi_- - \Gamma_- \Xi_+) \Big[\big(t^\dagger_{3\mu} t_{2\mu} (t^\dagger_{2\nu} + t_{2\nu}) + (\mu \leftrightarrow \nu) \big) + \text{h.c.} \Big] \\ & + (\Xi_+^2 + \Xi_-^2) \Big[t^\dagger_{3\mu} t_{1\mu} (t^\dagger_{3\nu} t_{1\nu} + t^\dagger_{1\nu} t_{3\nu}) + \text{h.c.} \Big] \\ & + (\Gamma_+^2 + \Gamma_-^2) \Big[t^\dagger_{3\mu} t_{2\mu} (t^\dagger_{3\nu} t_{2\nu} + t^\dagger_{2\nu} t_{3\nu}) + \text{h.c.} \Big] \\ & - (\Gamma_+ \Xi_- + \Gamma_- \Xi_+) \Big[\big(t^\dagger_{3\mu} t_{1\mu} (t^\dagger_{3\nu} t_{2\nu} + t^\dagger_{2\nu} t_{3\nu}) + (\mu \leftrightarrow \nu) \big) + \text{h.c.} \Big] \Big\}. \end{aligned} \tag{2.45}$$

For all numerical results, the Hamiltonian in the case $h_1 = h_2$ will be considered. It is obtained using the relations $u_- = 0$ and $v_- = 1$ which further imply $\Gamma_+ = \Gamma_- = v_+$ and $\Xi_+ = -\Xi_- = -u_+$. This significantly simplifies the Hamiltonian

$$\begin{aligned} H = &\sum_\nu \sum_{a=1}^{3} \epsilon_a t^\dagger_{a\nu} t_{a\nu} \\ &+ J_\parallel \sum_{\langle \mu,\nu \rangle} \Big\{ 2v_+^2 \left[t^\dagger_{1\mu} (t^\dagger_{1\nu} + t_{1\nu}) + \text{h.c.} \right] \\ &\qquad + 2u_+^2 \left[t^\dagger_{2\mu} (t^\dagger_{2\nu} + t_{2\nu}) + \text{h.c.} \right] \\ &\qquad - 2v_+u_+ \left[\left(t^\dagger_{3\mu} t_{1\mu} (t^\dagger_{1\nu} + t_{1\nu}) + (\mu \leftrightarrow \nu) \right) + \text{h.c.} \right] \\ &\qquad + 2v_+u_+ \left[\left(t^\dagger_{3\mu} t_{2\mu} (t^\dagger_{2\nu} + t_{2\nu}) + (\mu \leftrightarrow \nu) \right) + \text{h.c.} \right] \\ &\qquad + 2u_+^2 \left[t^\dagger_{3\mu} t_{1\mu} (t^\dagger_{3\nu} t_{1\nu} + t^\dagger_{1\nu} t_{3\nu}) + \text{h.c.} \right] \\ &\qquad + 2v_+^2 \left[t^\dagger_{3\mu} t_{2\mu} (t^\dagger_{3\nu} t_{2\nu} + t^\dagger_{2\nu} t_{3\nu}) + \text{h.c.} \right] \Big\}. \end{aligned} \tag{2.46}$$

The Hamiltonian in terms of independent hardcore bosons

Any model formulated with triplet operators can be rewritten in terms of independent hardcore bosons at the cost of introducing a density-density interaction. However, the dimer spectrum has the property that the third excitation is a combination of the first and the second, energetically

$$\epsilon_3 = \epsilon_1 + \epsilon_2, \tag{2.47}$$

which allows for suppressing the density-density interaction in H_0. Nevertheless, it will emerge in second order when the Hamiltonian is block-diagonalized. Starting from the triplet Hamiltonian in its form of Eq. 2.44 we proceed by substituting the operators $t_{1,2}$ by hardcore bosonic operators $b_{1,2}$. Processes involving the highest excitation t_3 are interpreted as processes involving both hardcore bosons simultaneously. In order to establish an exact correspondence, the processes are dressed with density terms as follows:

$$
\begin{aligned}
H =& \sum_{\mu} \sum_{a=1,2} \epsilon_a n_{a\mu} \\
&+ J_{\parallel} \sum_{\langle \mu,\nu \rangle} \Bigg\{ \Big[\Gamma_+ b^\dagger_{1\nu} + \Xi_- (1 - 2n_{1\nu}) b^\dagger_{2\nu} + \text{h.c.} \Big] \cdot \Big[\nu \rightarrow \mu \Big] \\
&\qquad + \Big[\Gamma_- (1 - 2n_{2\nu}) b^\dagger_{1\nu} + \Xi_+ b^\dagger_{2\nu} + \text{h.c.} \Big] \cdot \Big[\nu \rightarrow \mu \Big] \Bigg\}.
\end{aligned}
\tag{2.48}
$$

From multiplying out the products in the upper expression one finds the Hamiltonian decomposed into the fundamental quasi-particle processes:

$$
\begin{aligned}
H =& \sum_{\mu} \sum_{a=1,2} \epsilon_a n_{a\mu} \\
&+ J_{\parallel} \sum_{\langle \mu,\nu \rangle} \Bigg\{ \left(\Gamma_+^2 + \Gamma_-^2 \right) \Big[b^\dagger_{1\mu} \left(b^\dagger_{1\nu} + b_{1\nu} \right) + \text{h.c.} \Big] \\
&\qquad + \left(\Xi_+^2 + \Xi_-^2 \right) \Big[b^\dagger_{2\mu} \left(b^\dagger_{2\nu} + t_{2\nu} \right) + \text{h.c.} \Big] \\
&\qquad - 2\Gamma_-^2 \Big[\left(n_{2\mu} b^\dagger_{1\mu} \left(b^\dagger_{1\nu} + b_{1\nu} \right) + (\mu \leftrightarrow \nu) \right) + \text{h.c.} \Big] \\
&\qquad - 2\Xi_-^2 \Big[\left(n_{1\mu} b^\dagger_{2\mu} \left(b^\dagger_{2\nu} + b_{2\nu} \right) + (\mu \leftrightarrow \nu) \right) + \text{h.c.} \Big] \\
&\qquad + 4\Xi_-^2 \Big[n_{2\mu} n_{2\nu} b^\dagger_{1\mu} \left(b^\dagger_{1\nu} + b_{1\nu} \right) + \text{h.c.} \Big] \\
&\qquad + 4\Xi_-^2 \Big[n_{1\mu} n_{1\nu} b^\dagger_{2\mu} \left(b^\dagger_{2\nu} + b_{2\nu} \right) + \text{h.c.} \Big] \\
&\qquad + \left(\Gamma_+ \Xi_- + \Gamma_- \Xi_+ \right) \Big[\left(b^\dagger_{1\mu} \left(b^\dagger_{2\nu} + b_{2\nu} \right) + (\mu \leftrightarrow \nu) \right) + \text{h.c.} \Big] \\
&\qquad - 2\Gamma_+ \Xi_- \Big[\left(n_{1\nu} b^\dagger_{1\mu} \left(b^\dagger_{2\nu} + b_{2\nu} \right) + (\mu \leftrightarrow \nu) \right) + \text{h.c.} \Big] \\
&\qquad - 2\Gamma_- \Xi_+ \Big[\left(n_{2\mu} b^\dagger_{1\mu} \left(b^\dagger_{2\nu} + b_{2\nu} \right) + (\mu \leftrightarrow \nu) \right) + \text{h.c.} \Big] \Bigg\}.
\end{aligned}
\tag{2.49}
$$

Also this Hamiltonian will be used in its simplified form for the case $h_1 = h_2$:

$$\begin{aligned}
H = & \sum_{\mu} \sum_{a=1,2} \epsilon_a n_{a\mu} \\
& + J_{\parallel} \sum_{\langle \mu,\nu \rangle} \Big\{ 2v_+^2 \left[b_{1\mu}^\dagger (b_{1\nu}^\dagger + b_{1\nu}) + \text{h.c.} \right] \\
& \qquad + 2u_+^2 \left[b_{2\mu}^\dagger (b_{2\nu}^\dagger + b_{2\nu}) + \text{h.c.} \right] \\
& \qquad - 2v_+^2 \left[\left(n_{2\mu} b_{1\mu}^\dagger (b_{1\nu}^\dagger + b_{1\nu}) + (\mu \leftrightarrow \nu) \right) + \text{h.c.} \right] \\
& \qquad - 2u_+^2 \left[\left(n_{1\mu} b_{2\mu}^\dagger (b_{2\nu}^\dagger + b_{2\nu}) + (\mu \leftrightarrow \nu) \right) + \text{h.c.} \right] \\
& \qquad + 4u_+^2 \left[n_{2\mu} n_{2\nu} b_{1\mu}^\dagger (b_{1\nu}^\dagger + b_{1\nu}) + \text{h.c.} \right] \\
& \qquad + 4u_+^2 \left[n_{1\mu} n_{1\nu} b_{2\mu}^\dagger (b_{2\nu}^\dagger + b_{2\nu}) + \text{h.c.} \right] \\
& \qquad - 2v_+ u_+ \left[\left(n_{1\nu} b_{1\mu}^\dagger (b_{2\nu}^\dagger + b_{2\nu}) + (\mu \leftrightarrow \nu) \right) + \text{h.c.} \right] \\
& \qquad + 2v_+ u_+ \left[\left(n_{2\mu} b_{1\mu}^\dagger (b_{2\nu}^\dagger + b_{2\nu}) + (\mu \leftrightarrow \nu) \right) + \text{h.c.} \right] \Big\} .
\end{aligned} \tag{2.50}$$

The derived Hamiltonians for the frustrated transverse-field Ising bilayer are the starting point for the computation of deepCUT results. Even though they take less compact forms than in the original spin formulation, the decomposition in fundamental quasi-particle processes serves as the expansion in the basis of monomials in terms of which deepCUT is implemented. A detailed explanation of deepCUT is given in the next chapter.

3 Directly evaluated enhanced perturbative continuous unitary transformations

3.1 The method in context

The enhanced perturbative continuous unitary transformation (epCUT) and the directly evaluated epCUT (deepCUT) was introduced by Krull et al. in 2012 [10] as an extension of the perturbative unitary transformation (pCUT). PCUTs are only applicable to models having an equidistant spectrum in their perturbative starting point. This allows for an analytical solution of the flow equation up to arbitrary finite perturbative orders. EpCUTs are an enhancement of pCUT in the sense that they overcome the limitation to equidistant spectra at the cost that the perturbatively expanded flow equation can only be solved numerically. Also, in contrast to pCUT there exists no linked-cluster approach to neither epCUT nor deepCUT. Hence, perturbative series from epCUT must be expected to be less conclusive than state-of-the-art pCUT results close to quantum critical points, since here high orders are essential for capturing the effect of long-ranged quantum fluctuations. For deepCUT, the flow equation is not expanded perturbatively but it is evaluated directly. This makes deepCUT a close relative of self-similar continuous unitary transformations (sCUTs) which also stem from solving the flow equation directly. The difference to deepCUT is that the typically infinite flow equation is truncated by the choice of a finite operator basis according to an arbitrary scheme. DeepCUT specifies the truncation scheme by neglecting all basis terms which are not necessary in order to obtain the corresponding series with epCUT. In addition, individual terms in the flow equation are neglected if they do not influence the result up to the sought perturbative order. This is beyond a truncation just in terms of the basis. Hence, the flow equation for deepCUT is smaller than the smallest possible sCUT flow equation capturing the perturbative result exactly. Krull et al. stress that this truncation makes deepCUT canonical as compared to self-similar CUTs since only one parameter – the perturbative order – determines the truncation, and that the range of convergence is largely extended out of the perturbative parameter regime.

3.2 General derivation

We start the derivation of deepCUT by splitting the Hamiltonian into an exactly solvable part H_0 and a perturbation V

$$H = H_0 + xV. \tag{3.1}$$

In the context of flow equations a one-parameter family of Hamiltonians $H(l)$ with $0 \leq l < \infty$ is considered. $H(0) := H$ is the starting condition for the flow equation

$$\partial_l H(l) = [\hat{\eta}[H(l)], H(l)] \tag{3.2}$$

defining $H(l)$ for all finite values of l and the sought block-diagonal effective Hamiltonian $H_{\text{eff}} := H(\infty)$. The only choice to be made is the form of the superoperator $\hat{\eta}$ which is defined in terms of the basis of normal-ordered monomials (monoms) of second-quantization operators $A_i = b_{i_1}^{(\dagger)} \dots b_{i_n}^{(\dagger)}$ as

$$\hat{\eta}[A_i] = \text{sign}(\Delta E_i) A_i \tag{3.3}$$

where ΔE_i is the change of energy with respect to H_0 when A_i is applied to a state. Importantly, we have $\text{sign}(0) = 0$ such that diagonal monoms are not suppressed by the flow. To set up the flow equation, the Hamiltonian is written in the basis of monoms

$$H = \sum_i h_i A_i \tag{3.4}$$

with coefficients h_i. The flow equation expanded in this basis reads

$$\sum_i \partial_l h_i(l) A_i = \sum_{ijk} h_j(l) h_k(l) [\hat{\eta}[A_j], A_k]. \tag{3.5}$$

The commutator can be rewritten in second quantization as

$$[\hat{\eta}[A_j], A_k] = \sum_i D_{ijk} A_i \tag{3.6}$$

by introducing the symbols D_{ijk} correspondingly which then allow to set up the flow equation without operators

$$\partial_l h_i(l) = \sum_{jk} D_{ijk} h_j(l) h_k(l) \tag{3.7}$$

which can be solved numerically if the basis is finite.

3.2.1 Perturbative expansion and reduction of the flow equation

In order to calculate the coefficients of a perturbative series numerically stable, the flow equation must be expanded. We start with the perturbative expansion of the Hamiltonian

$$H(l) = \sum_{m=0}^{n} H^{(m)}(l) + \mathcal{O}\left(x^{n+1}\right) \tag{3.8}$$

$$= \sum_{m=0}^{n} x^m \sum_i f_i^{(m)}(l) A_i + \mathcal{O}\left(x^{n+1}\right). \tag{3.9}$$

In terms of the newly introduced coefficients $f_i^{(m)}$ the flow equation reads

$$\partial_l f_i^{(m)}(l) = \sum_{jk} \sum_{p+q=m} D_{ijk} f_j^{(p)}(l) f_k^{(q)}(l). \tag{3.10}$$

It can be solved numerically in order to gain the series expansion of any matrix element of the effective Hamiltonian, such as the vacuum energy per site

$$\langle 0 | H_{\text{eff}} | 0 \rangle = \sum_{m=0}^{n} x^m f_i^{(m)}(\infty) + \mathcal{O}(x^{n+1}) \tag{3.11}$$

for the monom i with $A_i = \mathbb{1}$. The choice of a targeted quantity specifies for which matrix elements of the effective Hamiltonian the series expansion is required. For any such targeted quantity and any order n the contributions D_{ijk} which are strictly necessary to obtain the correct expansion can be identified and all others can be neglected. In particular, this also reduces the basis $\{A_i\}$ to the minimal necessary basis if those monoms are dropped whose coefficients do not influence the targeted ones via the reduced set of contributions D_{ijk}. For the evaluation of a series expansion in the case of epCUT, the reduction of the equation is merely an optional optimization reducing the size of the differential equation system which must be solved numerically.

3.2.2 Direct evaluation of the flow equation

For deepCUT the reduced set of contributions defines the outcome in contrast. The flow equation is set up as in Eq. 3.7 but with necessary contributions only. Matrix elements can be obtained directly as for example the vacuum energy with $A_i = \mathbb{1}$

$$\langle 0|H_{\text{eff}}|0\rangle = h_i(\infty) + \mathcal{O}(x^{n+1}). \tag{3.12}$$

The error in the latter equation is expected to be significantly smaller than for epCUT. The coefficients $h_i(\infty)$ in general cannot be written as a series up to order n, but rather yield an infinite series if tailored. Hence, one finds

$$\sum_{m=0}^{n} x^m f_i^{(m)}(\infty) + \mathcal{O}(x^{n+1}) = h_i(\infty) \tag{3.13}$$

showing that the deepCUT result contains all information about the series from epCUT and additionally, a non-perturbative extrapolation resembling the true value for h_i in the effective Hamiltonian. This extrapolation depends on the truncation of the differential equation system and Krull et al. have shown that the truncation for deepCUT extends the range of convergence as compared to the series from epCUT [10].

3.3 Implementation for lattice models

The generality of the derivation above sheds light on the generality of the approach of deepCUT. All model specifics, such as the underlying algebra of second-quantization operators or the geometry of the problem are hidden in the calculation of commutators. In this section, these details will be explained for the case of lattice models in the thermodynamic limit. Here, it will also be pointed out how the truncation of deepCUT can be established practically. In the formal description in the previous section, the truncation has only been defined in terms of the infinite epCUT flow equation which one has no access to prior to the calculation of the commutators D_{ijk}. One therefore needs a scheme to stop the calculation of commutators at some point after all relevant monoms for the given perturbative order have been found. Furthermore, the discussion will also give evidence in which sense deepCUT is said to act in the thermodynamic limit, being considered one of the advantages of deepCUT over other methods such as NLCE.

Performing deepCUTs consists of two steps. First, all relevant commutators must be calculated and stored as the symbols D_{ijk}. Typically, this part limits the performance of deepCUT and it is carried out for general parameters of H_0 and a general perturbative parameter x. Moreover, this step is identical for epCUT and deepCUT. In the second, step the flow equation is set up explicitly to be solved numerically. Here, all parameters must be fixed and distinct equations are needed for epCUT and deepCUT. Hence, for any data point the differential equation is solved individually. Calculating the symbols D_{ijk} for general parameters of H_0 comes with the challenge that the generator cannot be determined unambiguously. In the currently available implementation we are able to treat two superimposed ladder spectra at most. This can be done either by two independent hardcore-bosons per site or by three triplonic excitations with $e_3 = e_1 + e_2$. Before one fixes the energies e_1 and e_2, one cannot tell whether for example the monom $b_{1i}b_{1j}b^\dagger_{2i}$ creates or annihilates energy or whether it is even block diagonal with vanishing generator. Therefore, the sign of these contributions can only be fixed in the second step when the flow equation is solved numerically.

3.3.1 Strategy for calculating commutators

Necessary inputs to the first step in the algorithm are the system Hamiltonian and the sought perturbative order n. The Hamiltonian $H(l = 0)$ is provided in the form

$$\{(A_i, O_{\mathrm{min}}(A_i))|i = 0, \dots, K\} \tag{3.14}$$

where K is the number of monoms occurring in the Hamiltonian at the beginning of the flow. The integer $O_{\mathrm{min}}(A_i) \in \mathbb{N}$ holds the information what is the leading order in the expansion

$$h_i(l, J) = \sum_{m=O_{\mathrm{min}}(A_i)}^{\infty} f_i^{(m)}(l)x^m \tag{3.15}$$

for any monom A_i. It is stored during the computation since it later defines the maximally reduced flow equation. In the initial Hamiltonian it also defines which monoms are in H_0 (typically counting operators) having a minimal order of 0, and which are in V (typically pair creation and annihilation and hopping terms) having an minimal order of 1. In order to store operators in lattice systems, translational invariance must be exploited. In general, symmetry-related monoms will at any point in the flow have equal prefactors. Hence, it is sufficient to only consider the symmetric superposition of all symmetry-related monoms as a representative of the corresponding symmetry class. This can be done for all symmetries equivalently which are the lattice symmetries and Hermiticity of the Hamiltonian. The exact treatment of symmetries will be explained later. For translational invariance the sum over lattice sites cannot be stored explicitly. Instead, a single summand without a specific site index is considered. All indices occurring in the representative are stored as vectors relative to a reference site. Strictly, from all symmetries only the incorporation of translational invariance is a prerequisite for the algorithm since it reduces the starting Hamiltonian to finitely many monoms. Since this superposition is never lifted, the whole algorithm can be considered to act in the thermodynamic limit. However, if one chose to calculate on a finite but sufficiently large cluster without exploiting any symmetry, the exact epCUT and even deepCUT results would be recovered, theoretically. Only the performance would be largely decreased. Keeping the sums over sites for clarity, e.g. for the TFIM the list of monoms and the corresponding minimal orders is initialized as follows:

Index i	Monom A_i	$O_{\min}(A_i)$
0	$\sum_i n_i$	0
1	$\sum_{\langle ij\rangle} b_i^\dagger b_j^\dagger + \text{h.c.}$	1
2	$\sum_{\langle ij\rangle} b_i^\dagger b_j + \text{h.c.}$	1

Here, rotational symmetry, inversion symmetry and the Hermiticity of the terms in the Hamiltonian are additionally incorporated which is done by storing the superposition of all symmetry related terms explicitly. Starting from that list, the algorithm calculates mutual commutators of all monoms and adds new contributions to the list with their respective minimal order. We only consider models with particle-number-conserving H_0, implying

$$\hat{\eta}[H_0] = 0. \tag{3.16}$$

This is important since otherwise commutators from $[\hat{\eta}[H_0], H_0]$ may give rise to new monomials of minimal order 0. These monoms would again contribute to the commutator and the procedure would have to be iterated until no new monoms occur, which is in general not guaranteed to take place. Then, custom truncation rules must be added for a self-consistent evaluation as for sCUT [22]. With the assumption in Eq. 3.16, the lowest contributing monoms have minimal order 1 and stem from

$$[\hat{\eta}[V], H_0]. \tag{3.17}$$

In general, also here multiple iterations to reach self-consistency may be necessary. However, if H_0 is local and the local Hilbert space is finite, self-consistency is guaranteed to be reached. Furthermore, for the hardcore-bosonic and triplonic algebras and H_0 being a sum of counting operators, relations like $bn = b$ prohibit the generation of any new monoms such that for all models considered in this thesis no self-consistent evaluation is applied and only one iteration is carried out in order to determine the contributions D_{ijk}. Still, the code for this project is capable of performing multiple iterations of the second kind under the assumption that self-consistency is reached after a finite number of iterations. After all, the first new monoms stem from the commutator

$$[\hat{\eta}[V], V] \tag{3.18}$$

and have a minimal order of 2 and a larger spatial extent than the monoms of first order. For example for the TFIM on the square lattice the commutator

$$\begin{aligned}[\hat{\eta}[A_1], A_2] &= \left[\sum_{\langle ij\rangle} b_i^\dagger b_j^\dagger - \text{h.c.}, \sum_{\langle ij\rangle} b_i^\dagger b_j + \text{h.c.}\right] \\ &= -2 \sum_{\langle\langle ijk\rangle\rangle} b_i^\dagger b_k^\dagger + \text{h.c.} + 4 \sum_{\langle\langle ijk\rangle\rangle} b_i^\dagger n_j b_k^\dagger + \text{h.c.}\end{aligned} \tag{3.19}$$

yields several new monoms where double brackets $\langle\langle ijk\rangle\rangle$ denote next-nearest neighbors i, k with intermediate site j. After all new monoms from the commutator in Eq. 3.18 have been calculated, they are added to the list of monoms. The last contributions from order 2 stem from commutators of these new monoms with monoms of order 0. Again, no self-consistent evaluation is needed and no new monoms arise. Having identified all monoms with minimal order 2, the same procedure is repeated in order to find the monoms with minimal order 3. In general, monoms of order n are calculated based on the monoms of all lower orders. The overall algorithm is illustrated in Fig. 3.1. $H^{(n)}$ contains all monoms with minimal order n ($H^{(0)} = H_0$ and $H^{(1)} = V$) and $\eta^{(n)} := \hat{\eta}[H^{(n)}]$. The gray blocks correspond to those commutators neglected in the case of a block-diagonal H_0. The commutators for the evolution of $\partial_l H^{(n)}$ are first of all

$$[\eta^{(1)}, H^{(n-1)}],\ [\eta^{(2)}, H^{(n-2)}], \ldots,\ [\eta^{(n-1)}, H^{(1)}] \tag{3.20}$$

which contain only monoms from previous orders. After all new monoms from these commutators are calculated and added to the list, the last block of commutators for order n

$$[\eta^{(n)}, H^{(0)}] \tag{3.21}$$

can be calculated – if necessary self-consistently. If new monoms arose they would be added to the list and the next order can be calculated. This

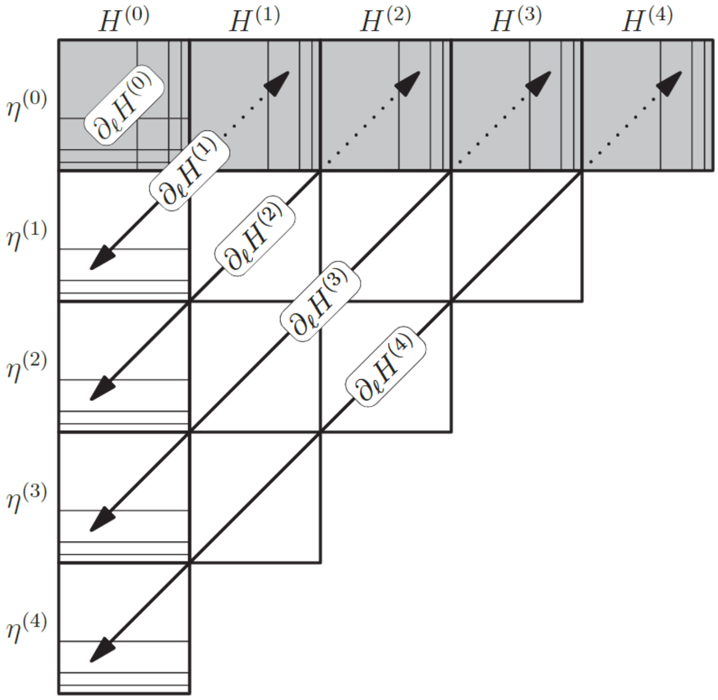

Figure 3.1: Illustration of the algorithm calculating the commutators for deepCUT. Horizontally, all monoms are listed with increasing minimal order and vertically those contributing to the generator. The algorithm iterates over orders m up to the order at which the truncation is applied. In each iteration commutators of monoms in the blocks $\eta^{(q)}$ and $H^{(p)}$ are calculated if $q + p = m$, which yield the contributions determining the flow equation in order m. Additional lines in the blocks signify the need for self-consistent evaluation and must be treated last in their order. The gray blocks are excluded if H_0 is energy-conserving.

structured way of going from low to high orders allows us to terminate the algorithm at any finite order since the number of monoms is guaranteed to be finite due to the bounded spatial extent of the monoms combined with the finite local Hilbert space. One caveat of the implementation is that each pair of monoms A_i, A_j may contribute to two commutators. If a new monom A_k arises in both commutators but with opposite sign, e.g.

$$D_{kij} = -D_{kji} \tag{3.22}$$

it cancels out in the flow equation. Keeping the monom would not disturb the result immediately, but for the correct truncation it is necessary to use the properly increased minimal order for A_k which is practically done by removing it from the list of monoms after each update of the list. However, as mentioned earlier, the sign of the contributions is ambiguous before the parameters of the two ladder spectra are fixed. That is why in our implementation this step is omitted. In the second step after the sign is fixed, mutually cancelling contributions are removed, but there is no correction of the potentially too low minimal order anymore. In that case our flow equation is no longer guaranteed to be minimal. We expect the deviations as compared to standard deepCUT small whatsoever, and the epCUT results are not affected at all. Similar observations have been made by Drescher [31]. He emphasizes that for the mentioned reasons the minimal order does not strictly agree with the leading order in the expansion for practical implementations of deepCUT. He further points out that hidden symmetries in the flow may further disturb the correspondence for which cannot be corrected at all.

Summarizing, the necessary return values of the first step of the algorithm are the commutator symbols D_{ijk}, the information by which amount monom i changes the energy in units of e_1 and e_2 and the minimal orders for all monoms.

3.3.2 Setting up and reducing the flow equation

The goal of the second step of the algorithm is to set up either the epCUT or deepCUT flow equation based on the information calculated in the first step. As pointed out in the derivation, the epCUT flow equation must be set up anyways in order to establish the correct truncation. We emphasize that the minimal flow equation is defined with respect to a targeted quantity. This is either the ground-state energy E_0 or the dispersion yielding the energy gap Δ, within the scope of this thesis. The targeted quantity is passed to the algorithm as sets of matrix elements one is interested in:

$$\begin{array}{ll} \{\mathbb{1}\} & \text{for } E_0, \\ \{b_i^\dagger b_j \,|\, |i-j| \leq n\} & \text{for } \Delta. \end{array} \tag{3.23}$$

Additionally to the known minimal orders, one asks now for each monom what is the highest order $O_{\max}(A_i)$ which still influences any targeted quantity in order n or lower. For the targeted quantities themselves this is straightforwardly n. For all other monoms the maximal order can be determined iteratively using the structure of the flow equation as encoded in D_{ijk}. This is done via the formal definition

$$O_{\max}(A_j) = \max_{\{i,k | D_{ijk} \neq 0 \,\vee\, D_{ikj} \neq 0\}} \left(O_{\max}(A_i) - O_{\min}(A_k)\right). \tag{3.24}$$

The initial set of maximal orders is defined as

$$O_{\max}(A_i) = \begin{cases} n \text{ if } A_i \text{ targeted} \\ 0 \text{ else} \end{cases} \tag{3.25}$$

which is plugged into the right-hand side of Eq. 3.24. This increases the maximal orders monotonously in each iteration. The break-off condition is that the maximal orders do not change anymore which is guaranteed to take place for finitely many monoms at finite targeted order n. Then, the flow equation of epCUT

$$\partial_l f_i^{(m)}(l) = \sum_{jk} \sum_{q+p=m} D_{ijk} f_j^{(q)}(l) f_k^{(p)}(l) \tag{3.26}$$

is set up with the restrictions

$$O_{\min}(A_i) \leq m \leq O_{\max}(A_i), \tag{3.27}$$

$$O_{\min}(A_j) \leq q \leq O_{\max}(A_j), \tag{3.28}$$

$$O_{\min}(A_k) \leq p \leq O_{\max}(A_k). \tag{3.29}$$

This implies that monoms with $O_{\mathrm{min}} > O_{\mathrm{max}}$ are discarded, as well as contributions D_{ijk} with $O_{\mathrm{max}}(A_i) < O_{\mathrm{min}}(A_j) + O_{\mathrm{min}}(A_k)$. The deepCUT flow equation is then built uniquely from all monoms and contributions which have not been discarded in the epCUT flow equation. This reduction step still can be done once for all before the parameters for the energy ladders in H_0 are fixed.

This finally is done together with fixing the perturbative parameter x in order to solve the equation numerically. When the equation is set up, for each contribution D_{ijk} it is checked whether the monom j changes the energy at all, otherwise the contribution is left out. If it changes the energy, D_{ijk} is dressed with the appropriate sign depending on whether the monom increases or lowers the energy. After this step is done, the flow equation is checked for cancellations of the form

$$D_{kij} = -D_{kji} \tag{3.30}$$

which allow to reduce the equation further. In the condition for equal energies a numerical threshold of 1×10^{-10} in the corresponding unit of energy is used.

3.4 Implementation details and optimizations

3.4.1 Symmetries

The performance of the implementation heavily relies on using the symmetries of the physical model. Each monom shares its prefactor at any point in the flow with all monoms it can be transformed to by symmetry transformations, and it is more performant to track only a single prefactor for each set of symmetry-related monoms. Therefore, from now on the term monom will refer to the symmetric superposition of itself with all local monoms in that set. These are created by omitting the sums for translational invariance and considering only relative positions to a reference site, allowing for computations in the thermodynamic limit. The other symmetries are rotation and inversion symmetry, depending on the lattice, and the constraint of Hermiticity $A_i^\dagger = A_i$. These symmetries are implemented by storing the contributing local monoms explicitly. For example the pair creation and annihilation of a flavor-one and a flavor-two particle would read

$$\sum_{\langle\mu\nu\rangle}(t_{1\mu}t_{2\nu}+t_{2\mu}t_{1\nu})+\text{h.c.} \tag{3.31}$$

and be represented internally by

$$\sum_{\delta_{\text{NN}}} t_{1\mu}t_{2(\mu+\delta_{\text{NN}})}+\text{h.c.} \tag{3.32}$$

using lattice vectors δ_{NN} connecting a site with all its nearest neighbors. The sum over μ is suppressed to emphasize that it is a symbolic index. Note that the reflection symmetry in this case is covered by the rotations. Algorithmically, all symmetries other than the translational symmetry are implemented as functions which take a local monom and return a symmetric superposition of local monoms related by the symmetry. The global prefactor of the superposition is not necessarily one since a local monom can be mapped to itself by a symmetry transformation. A paradigmatic example is the particle number operator

$$\text{sym}_{\triangle}[t^{\dagger}_{\nu 1}t_{\nu 1}] = 24\, t^{\dagger}_{\nu 1}t_{\nu 1}, \tag{3.33}$$

where $\text{sym}_{\triangle}$ applies the symmetry transformations of the triangular lattice – again discarding the translational invariance. From the reflection symmetry a factor of 2, from the rotation symmetry a factor of 6 and a factor of 2 from Hermiticity generate an overall factor of 24. These factors will be referred to as symmetry factors s_i for each monom A_i. By the convention of Krull et al. the monoms are defined with prefactors of one such that formally the symmetry factors will not be considered part of the monom, implying

$$\text{sym}[a_i] = s_i A_i \tag{3.34}$$

for any local monom a_i contributing to A_i.

3.4.2 Expanding commutators of monoms efficiently

At its heart, the deepCUT algorithm iteratively takes pairs of monoms (A_j, A_k), calculates their mutual commutator $[A_j, A_k]$. After normal-ordering the result can be expressed as

$$[A_j, A_k] = \sum_i D_{ijk} A_i, \tag{3.35}$$

which is known to be symmetric. Hence, it can be expanded in monoms by iteratively considering a contributing local monom and identifying all symmetry-related local monoms in the result, removing them and storing the common prefactor in the structure coefficients. This procedure leaves plenty of room for optimizations. Introducing the corresponding symmetry factors, the commutator above can be rewritten as

$$[s_j A_j, s_k A_k] = \big[\mathrm{sym}[a_j], \mathrm{sym}[a_k]\big] = \mathrm{sym}\Big[\big[a_j, \mathrm{sym}[a_k]\big]\Big], \tag{3.36}$$

where $a_{j,k}$ again denote arbitrary local monoms of $A_{j,k}$. Due to the bilinearity of the commutator, one of the sums introduced by the sym-operations can be applied on the result of the commutation with a local monom. This saves exactly as many terms in the computationally costly process of normal ordering as generated by the symmetry operation. It is not even necessary to restore the result by applying the symmetries after the commutation. Instead, Eq. 3.34 can be used to extract the structure coefficients from the unsymmetrized result. To see that, a monom A_i is rewritten in terms of local monoms as $\sum_n a_i^n$, yielding

$$\big[a_j, \mathrm{sym}[a_k]\big] = \sum_{i,n} c_i^n a_i^n \,. \tag{3.37}$$

It is noteworthy that many of the introduced coefficients c_j^n are expected to be zero if A_j consists of many local operators. Reinserting into Eq. 3.36, one finds

$$[s_j A_j, s_k A_k] = \sum_{i,n} c_i^n \mathrm{sym}[a_i^n] = \sum_{i,n} c_i^n s_i \, A_i. \tag{3.38}$$

Comparing this with Eq. 3.35 directly implies

$$D_{ijk} = \frac{s_i}{s_j s_k} \sum_n c_i^n \tag{3.39}$$

which allows for the computation of the structure coefficients involving only the symmetrization of a single monom if all symmetry factors are known.

This is implemented by storing the monoms directly in the form $s_i A_i$. In the implementation, it turns out that it is natural to introduce an additional factor of $s_j s_k$ in Eq. 3.36 by replacing a_j, a_k by $s_j a_j, s_k a_k$. The final result is then changed to

$$D_{ijk} = \frac{s_i}{s_j^2 s_k^2} \sum_n c_i^n . \tag{3.40}$$

It is important to note that for the expansion of the commutator in monoms and the identification of new monoms, any arising term must be looked for in the current list of monoms. This is costly for high orders since this list becomes long. Alexander Reischl came up with the idea to use a hash function mapping a monom to its index in the list to avoid the search processes. Being an overhead for low orders, this speeds up the algorithm in high orders significantly. We use the standard string hash function of the first summand of each monom as outputted text. Another comment for better readability of the code is that the constraint of Hermiticity is treated differently from other symmetries. For any operators X, Y one finds

$$[X - \text{h.c.}, Y + \text{h.c.}] = [X, Y + \text{h.c.}] + \text{h.c.} \tag{3.41}$$

Hence, Hermiticity being not model-specific is more easily treated on an analytical level than by using the symmetry operations.

3.4.3 Commutator and normal ordering for hardcore bosons

An algorithmically challenging step is the mutual commutator between two representatives of two monoms. The challenge is that the sums for translational invariance are not stored explicitly and therefore, any relative position between the two representatives must be considered. Alexander Reischl has formulated the following approach in his PhD thesis [32]. For two representatives

$$A = A_{i+\delta_1} A_{i+\delta_2} \ldots A_{i+\delta_M}, \qquad B = B_{j+\delta'_1} B_{j+\delta'_2} \ldots B_{j+\delta'_N} \tag{3.42}$$

with independent reference sites i and j and creation or anihilation operators $A_{i+\delta_n}$ on the sites $i + \delta_n$ for $n = 1, \ldots, M$ and for B equivalently. The commutator $[A,B]$ can be rewritten using a product rule for commutators as

$$\sum_{m=1}^{M}\sum_{n=1}^{N} A_{i+\delta_1}\dots A_{i+\delta_{m-1}} B_{j+\delta'_1}\dots B_{j+\delta'_{n-1}} \left[A_{i+\delta_m}, B_{j+\delta'_n}\right] B_{j+\delta'_{n+1}}\dots B_{j+\delta'_N} A_{i+\delta_{m+1}}\dots A_{i+\delta_M}. \tag{3.43}$$

The remaining commutator in each summand is a commutator of two creation or annihilation operators which is given by the commutation relation of the algebra directly, as for example for hardcore bosons

$$\left[b_i, b_j\right] = \left[b_i^\dagger, b_j^\dagger\right] = 0, \tag{3.44}$$

$$\left[b_i, b_j^\dagger\right] = -\left[b_i^\dagger, b_j\right] = \delta_{ij}(1-2n_i). \tag{3.45}$$

Importantly, the commutator in Eq. 3.43 is either zero or proportional to a Kronecker symbol

$$\delta_{i+\delta_m, j+\delta'_n} \tag{3.46}$$

which fixes the relative position of the reference site i and j by

$$j = i + \delta_m - \delta'_n \tag{3.47}$$

for each summand. After the replacement the result is of the form

$$C = C_{i+\delta''_1} C_{i+\delta''_2} \dots C_{i+\delta''_K} \tag{3.48}$$

and still must be normal-ordered in order to be expanded in terms of normal-ordered monoms eventually. Strictly speaking, the monoms are not normal-ordered but site ordered, and only operators on the same site are normal-ordered. The algorithm is designed specifically for hardcore particles. In the case of two independent hardcore bosons, different flavors are considered as different sites and in the case of triplons, different flavors must be treated on the same site. This increases the efficiency since one saves on evaluations of the elementary commutator which is always zero for operators on different sites. Hence, the algorithm to normal order C starts with a stable sort with respect to the lattice index guaranteeing that the order of operators on the same site is not changed. Next, in a loop over sites occurring in C for each local product it is checked whether the whole product is zero due to one of the following properties of hardcore bosons

$$t_a t_b = t_a^\dagger t_b^\dagger = 0 \text{ for all } a, b \tag{3.49}$$

$$t_a t_b^\dagger = 0 \text{ for } a \neq b. \tag{3.50}$$

Indices a, b denote the flavor, and the site index is suppressed since we consider a local product on one site. The notation resembles triplonic operators but is also applicable to standard hardcore bosons if one allows only for one flavor. If C is not zero according to these heuristics, in a second loop over all sites a normal-ordering routine is applied to all local products. It distinguishes three cases corresponding to the length of the local product. If it is one the product is already normal ordered. If it is two the product can be of the form

$$t_a^\dagger t_b \tag{3.51}$$

which is normal ordered, or of the form

$$t_a t_a^\dagger = 1 - \sum_{\text{flavors } b} n_b \tag{3.52}$$

which can be replaced by the normal-ordered right-hand side. In the third case if the length of the local product is equal or greater than three, it takes one of the forms

$$t_a^\dagger (t_a t_a^\dagger)^m (t_b t_b^\dagger)^n t_b = t_a^\dagger t_b \tag{3.53}$$

$$t_a^\dagger (t_a t_a^\dagger)^m (t_b t_b^\dagger)^n = t_a^\dagger \tag{3.54}$$

$$(t_a t_a^\dagger)^m (t_b t_b^\dagger)^n t_b = t_b \tag{3.55}$$

$$(t_a t_a^\dagger)^m (t_b t_b^\dagger)^n = 1 - \sum_{\text{flavors } c} n_c \tag{3.56}$$

with $m + n \geq 1$. For the special case that the local product stems from two normal-ordered terms, as in our case, we can furthermore discard the fourth case and we know $m + n = 1$.

The algorithm above only works for hardcore particles with $n \in \{0, 1\}$ and the commutator relations are built in implicitly. Additionally, the code contains an alternative, more general recursive approach implemented by

Matthias Walther in which the algebra is well-separated. In the implementation used by Nils Drescher and Alexander Reischl, a third approach has been chosen. They calculate all possible local products and their respective normal-ordered result beforehand and store it in a look-up table for the later computation. This presumably requires more memory but saves computations as in the algorithm above. A comparison of the approaches has not been made.

3.4.4 Simplification rules

In the calculation of commutators for epCUT and deepCUT the most important optimization is the introduction of model-specific simplification rules [10]. They are heuristics which avoid the computation of contributions and monoms which would later be discarded in the reduction of the differential equation system which strictly can only be carried out after all potentially contributing monoms and their minimal orders have been found. Krull et al. distinguish between two kinds of simplification rules. *A posteriori rules* are applied after the calculation of a commutator

$$[\hat{\eta}[A_j], A_k] = \sum_k D_{ijk} A_i \tag{3.57}$$

to all resulting monoms A_i which are new at that point in the algorithm. Roughly speaking, if they contain too many creation or annihilation operators they cannot be reduced to a targeted quantity by repeated commutations with other monoms without exceeding the targeted order. In that sense, *a posteriori* rules give an upper bound for the maximal order of a monom depending on the targeted quantities and reduce the number of monoms stored during the computation and therefore also the number of total commutators in total largely. The second kind of simplification rules are *a priori* rules. They are applied to a pair of monoms before their mutual commutator is calculated. They estimate the size of the smallest possible resulting monom and discard the computation of the commutator if that monom is too big. That does not reduce the number of monoms further, but saves the computation of a large fraction of commutators. In this section, simplification rules for all relevant models will be presented. For single-layer

TFIMs they can be directly taken from earlier works on deepCUT [10, 27]. For the formulations of the bilayer TFIM modified versions of these rules have been found to be satisfactory.

In this section, all used simplification rules are stated. The derivation for previously known rules is not given. The basic idea of the derivation is that it is sufficient to consider commutation with the monoms in the perturbation at the beginning of the flow only. With each commutation the order is increased by one and the number of operators in the monom is decreased by a fixed number of operators at most. By counting the number of commutations at least necessary to reduce the monom to a targeted one, upper bounds for the maximal order can be obtained. In the following, we take n to be the targeted order. The number of creation or annihilation operators, which can at most be eliminated by a commutation with a monom of the perturbation V, is two for all our models. Furthermore, the number of targeted quasi-particles q encodes whether the ground-state energy ($q = 0$) or the energy gap ($q = 1$) is targeted. In the implementation, q is supplied to the first part of the algorithm as an additional parameter.

A posteriori rules

The *a posteriori* rules formulated in Ref. [10] give

$$\widetilde{O}_{\max} = n - \left\lceil \frac{\max(c-q,0)}{2} \right\rceil - \left\lceil \frac{\max(a-q,0)}{2} \right\rceil \geq O_{\max} \tag{3.58}$$

as an upper bound for the maximal order for a monom with c creation operators and a annihilation operators. For the single-layer TFIMs this bound has been observed to be very tight and almost optimal.

For the bilayer models in terms of triplons we find that the perturbation contains the terms $t_{1\mu}t_{1\nu}$ and $t_{2\mu}t_{2\nu}$, but no equivalent term for the third flavor. In second order however, the corresponding monom occurs from the combination

$$t^\dagger_{3\mu}t_{1\mu}t^\dagger_{3\nu}t_{1\nu} \cdot t^\dagger_{1\mu}t^\dagger_{1\nu} = t^\dagger_{3\mu}t^\dagger_{3\nu} + \dots \tag{3.59}$$

Therefore, two creation or annihilation operators of the third flavor can be cancelled only at the cost of two orders. Hence, with a_c and b_c denoting the number of annihilation and creation operators of flavor c, a simple improved rule can be formulated by counting operators of flavor 3 twice. Since there are no mixed terms like $t_{1\mu}t_{2\nu}$ in the symmetric model in first order, one can further apply the ceiling function to every flavor individually as

$$\begin{aligned}\tilde{O}_{\text{max}} = n - \left\lceil \frac{\max(c_1 - q, 0)}{2} \right\rceil - \left\lceil \frac{c_2}{2} \right\rceil - c_3 \\ - \left\lceil \frac{\max(a_1 - q, 0)}{2} \right\rceil - \left\lceil \frac{a_2}{2} \right\rceil - a_3\end{aligned} \quad (3.60)$$

if at most the one-particle sector is targeted.

For the bilayer model in terms of two independent hardcore bosons per site the rule from Eq. 3.58 holds, too. To make the bound sufficiently tight we make use of the the fact that a term like $b_{1\mu}b_{2\nu}$ cannot be cancelled at the cost of just one order in general. This only happens in situations like the following

$$n_{2\mu}b_{1\mu}b_{2\nu} \cdot b^{\dagger}_{2\mu}b^{\dagger}_{1\mu}b^{\dagger}_{2\nu} = b^{\dagger}_{2\mu} + \ldots \quad (3.61)$$

where the first term stems from the perturbation in order one and $b^{\dagger}_{1\mu}b^{\dagger}_{2\nu}$ from the second term is cancelled. The prerequisite for this to happen is that the monom contains a site with a term $b_{1\mu}b_{2\mu}$ or its hermitian conjugate. This is always fulfilled on a site with three operators or more or if the local operator is exactly $b_{1\mu}b_{2\mu}$ or the hermitian conjugate. The rule is formulated as follows. If there is any site in the monom allowing for mixed cancellation according to the conditions described above, we apply the rule

$$\tilde{O}_{\text{max}} \quad = \quad n - \left\lceil \frac{\max(c_1 - q, 0) + c_2}{2} \right\rceil - \left\lceil \frac{\max(a_1 - q, 0) + a_2}{2} \right\rceil . \quad (3.62)$$

Else, we apply the following rule:

$$\tilde{O}_{\text{max}} = n - \left\lceil \frac{\max(c_1 - q, 0)}{2} \right\rceil - \left\lceil \frac{c_2}{2} \right\rceil - \left\lceil \frac{\max(a_1 - q, 0)}{2} \right\rceil - \left\lceil \frac{a_2}{2} \right\rceil . \quad (3.63)$$

Moreover, for all models an extended simplification rule can be applied as introduced for two-dimensional systems in Ref. [27]. The idea is that for example two operators $b_\mu b_\nu$ cannot be cancelled at the cost of one order if they are not nearest neighbors. For the extended simplification rule the support of the monom is split into linked subclusters and by simple counting arguments a bound is determined, which is better than the ordinary bounds if the monom is sparsely distributed over the lattice. The rule has been taken over directly from Ref. [27] with a detailed explanation in the appendix. Our only modification is that we double count flavor-three triplons as in the standard rule for the triplonic bilayer.

A priori rules

As mentioned before, *a priori* rules are applied to a pair of monoms T, D of which the commutator is to be calculated. They give an upper bound for the maximal order of the resulting monoms. Krull et al. find

$$\begin{aligned}\widetilde{O}_{\max,TD} = n - &\left\lceil \max\left(\frac{c_T + c_D - \min(a_T, c_D)}{2} - q, 0\right)\right\rceil \\ &- \left\lceil \max\left(\frac{a_T + a_D - \min(a_T, c_D)}{2} - q, 0\right)\right\rceil \end{aligned} \tag{3.64}$$

with c_D and a_D being the number of creators and annihilators in the monom D. The sought upper bound is then given by

$$\widetilde{O}_{\max} = \max\left(\widetilde{O}_{\max,TD}, \widetilde{O}_{\max,DT}\right). \tag{3.65}$$

Extended *a priori* rules reflecting the real space structure of monoms as also introduced in Ref. [10] have not been implemented but would be expected to yield further improvement.

3.4.5 Alternative generator schemes

The particle-conserving generator which is the standard choice for pCUT and epCUT decouples all quasi-particle sectors. If however, as for many applications, the ground-state energy and the energy gap are sufficient, it is sufficient to decouple only the first block for the ground state or the first and second block for the energy gap from all others. This idea has been put forward by the introduction of the $0{:}n$ and $1{:}n$ generators [33]. Practically, the $0(1){:}n$ generator is implemented by only allowing for monoms in the generator which either have at most $0(1)$ creation operators or at most $0(1)$ annihilation operators. The resulting series is not affected by switching between the appropriate generators, but the size of the basis is decreased. Non-perturbative results from deepCUT are expected to be better using the standard generator [10]. However, the quantitative differences are small. The advantages are a performance boost from the decreased basis size and a potentially extended range of convergence of the deepCUT. Divergences are expected when energy levels of a higher quasi-particle block drop into the continuum of a lower-energy block. This induces a sign change in the generator following Eq. 3.3 which changes the exponential suppression of the corresponding monoms to an exponential increase, and the flow diverges in the limit of $l \to \infty$. All numerical results for the ground-state energy (energy gap) use the $0(1){:}n$ generator.

3.4.6 Parallelization

The calculation of commutators is well-parallelizable. All commutators can be calculated independently as long as the list of monoms is not needed to be updated. We apply the parallelization to the two for-loops over monoms in the generator and monoms in the Hamiltonian. We collect the results and update the results after each block

$$[\eta^{(p)}, H^{(q)}]. \tag{3.66}$$

All variables are stored in shared memory and the only critical step in the computation is when new entries are written into the map D_{ijk} which must not happen simultaneously from different threads.

3.4.7 Numerical solution of the differential equation

The numerical solution of the differential equation is found using the scipy library for python and the dopri5 solver [34]. The break-off condition detecting the convergence in the limit of infinite flow parameter is the residual off-diagonality (ROD) defined as

$$\sqrt{\sum_{\Delta E(A_i)\neq 0} h_i(l)^2} < \epsilon \tag{3.67}$$

where the sum contains all monoms which are aimed to be eliminated according to the selected generator. We terminate the flow at a ROD of 1×10^{-9} in the respective units of energy. Higher RODs are not accessible in the highest orders of deepCUT, likely due to the accumulated numerical error in the sum over squares if the number of monoms is large. The relative tolerance in the solver is set to 1×10^{-6}.

For the detection of a divergence in the flow, the minimal ROD which occurs in the flow from 0 to l is tracked. If the ROD exceeds the minimum at some point during the flow by a factor of 1×10^{8} or more, the deepCUT is considered to be non-convergent for the respective parameters.

4 Analysis of quantum criticality using deepCUT

4.1 Results for single-layer models

This section presents the numerical results obtained with deepCUT on the various models. The overall question is how the results can be used to access quantum critical properties. The problem becomes apparent looking at Fig. 4.1. The deepCUT result for the gap in the frustrated single-layer TFIM is shown for the highest available orders. The comparison with the also shown series results reveal that the range of convergence is extended by deepCUT as desired. That also means that the alternating structure in the series is suppressed by deepCUT. However, even in the highest orders the gap behaves linearly around its closing which means that it does not give direct access to the critical scaling. Furthermore, looking at the closing of the gap which is shown in the inset against the reciprocal order, alternating features still emerge in higher orders worsening the quality of extrapolations. If one tries to extrapolate by a linear fit to the data against the reciprocal order which has extensively been done for deepCUT in the uncritical regime, the result for the critical point is $J/h = 0.589$. This is off as compared to the best literature value of $J/h = 0.610(4)$ [30]. This is found to be due to the fact that the closing of the gap is supposed to scale linearly with respect to $n^{-1/\nu}$ rather than n^{-1} under the assumption that the approximate data is analytic. Using the insights on the proper scaling relations will turn out to be the key to extracting critical properties. We present different approaches to determine the critical exponent α from the deepCUT data for the ground-state energy E_0 and the critical exponents z and ν as well as the critical point J_c. In particular for the gap, some approaches are ill-suited for the

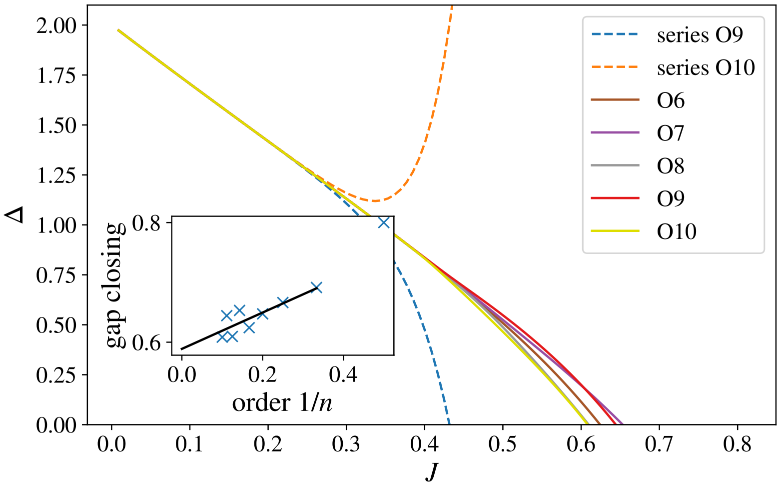

Figure 4.1: Typical results from deepCUT: the energy gap in the frustrated TFIM on the triangular lattice. The bare series is plotted in order 9 and 10 and can be compared to the deepCUT results from order 6 to 10, denoted by On. The series is alternating and converges slowly. DeepCUT extends the range of convergence and is more stable than the series even in the non-convergent region. The closing of the gap against the inverse order is shown in the inset. Assuming a linear relation does not allow for a precise extrapolation of the critical point. The behavior of the gap around the closing is strongly linear and does not give direct access to critical properties.

TFIMs we consider, as compared to others. We include them for the sake of completeness.

4.1.1 Analysis of the zero-temperature heat capacity

For the analysis of the critical non-analyticity in the ground-state energy, a scaling-based approach has been applied in the Bachelor's project of Markus Pirke [35]. The second derivative of the ground-state energy

$$\partial_J^2 E_0 \propto \frac{C}{J^2}, \tag{4.1}$$

being proportional to the heat capacity around the critical point, has been evaluated at the critical point using NLCE for the TFIM on the triangular lattice. They argue that at the critical point the second derivative should scale as

$$\partial_J^2 E_0 \sim n^{\frac{\alpha}{\nu}} \tag{4.2}$$

assuming the truncation in NLCE to be proportional to the length scale. They perform a power law fit to contributions per order with the expectation

$$\partial E_0^{(n)} - \partial E_0^{(n-1)} \sim n^{\frac{\alpha}{\nu}-1} \tag{4.3}$$

and find $\alpha = 0.08$ for the 3d Ising universality which is to be compared to $\alpha = 0.110087(12)$ from literature [36]. We adapt this method for deepCUT. A natural question is whether it is crucial to consider the contributions per order instead of the scaling of the observable itself. Using deepCUT data, we have not been able to find the correct scaling behavior without considering contributions per order. We assume this is due to corrections to the scaling of the heat capacity, which can be described by

$$\partial_J^2 E_0 \sim B + A\xi^{\frac{\alpha}{\nu}} \tag{4.4}$$

around the critical point as it has been done in Ref. [37]. The offset B is expected to bias the log-log fit for the detection of a power law. For $\alpha > 0$, as for the 3d Ising universality class, one at least can expect asymptotic convergence since $(J - J_c)^{-\alpha}$ diverges at the critical point and the offset is suppressed relatively. However, for the 3dXY universality class with negative $\alpha = -0.01526(30)$ [38], the value of the heat capacity at the critical point is finite and even the asymptotic limit is expected to be biased. For the case of the antiferromagnetic TFIM on the triangular lattice, the bias leads to an exponent with wrong sign and strongly overestimated absolute value, capturing the criticality not at all. Here, for both universality classes we perform fits of two kinds. First, we consider the approach by Markus Pirke and perform a linear fit in a log-log plot of contributions per order against order. Second, we consider the normal data, but fit a function of the form

$$f(n) = a + bn^c \tag{4.5}$$

with c capturing the scaling behavior. The cost of doing that is that one parameter more must be fixed by the data as compared to the log-log fit.

The results are shown in Figs. 4.2 – 4.4. The ferromagnetic model on the triangular lattice is shown in Fig. 4.2 where both variants of fitting are

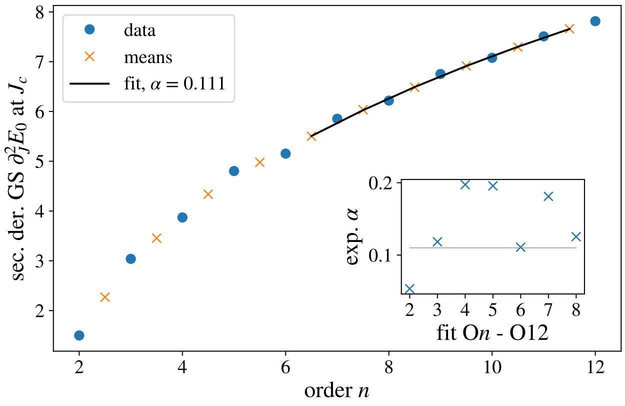

(a) Analysis by a power law fit.

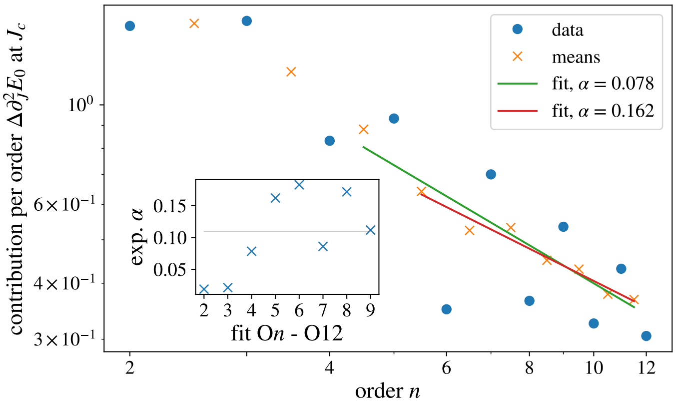

(b) Analysis of the contributions per order by a log-log fit.

Figure 4.2: Analysis of the ground-state energy in the ferromagnetic TFIM on the triangular lattice. The inset plot shows the values for α from fit windows from order n to 12. The change in even orders is way lower than in odd orders as is apparent in panel (b). The literature value $J_c = 0.20973$ [15] is used for the critical point.

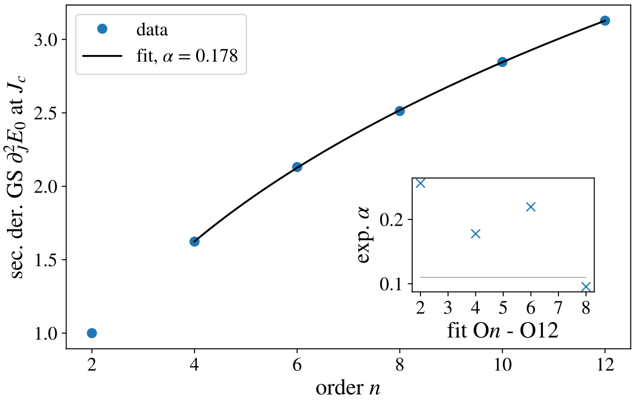

(a) Analysis by a power law fit.

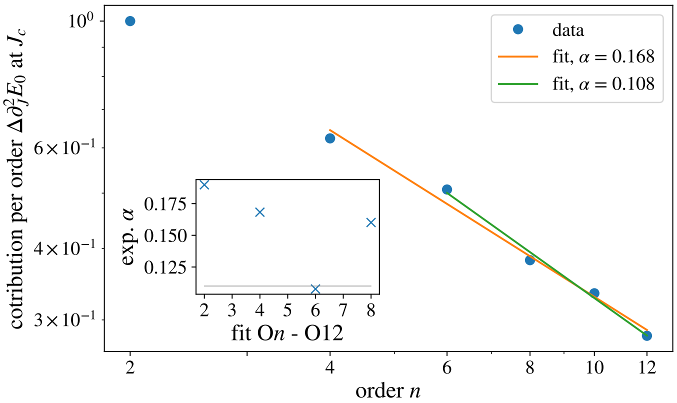

(b) Analysis of the contributions per order by a log-log fit.

Figure 4.3: Analysis of the ground-state energy in the ferromagnetic TFIM on the square lattice. New contributions arise only in even orders in analogy to the series. The value $J_c = 0.3284$ [15] is used for the critical point.

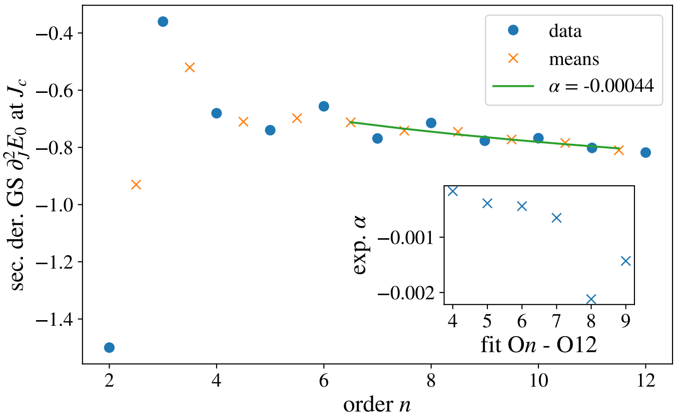

(a) Analysis by a power law fit.

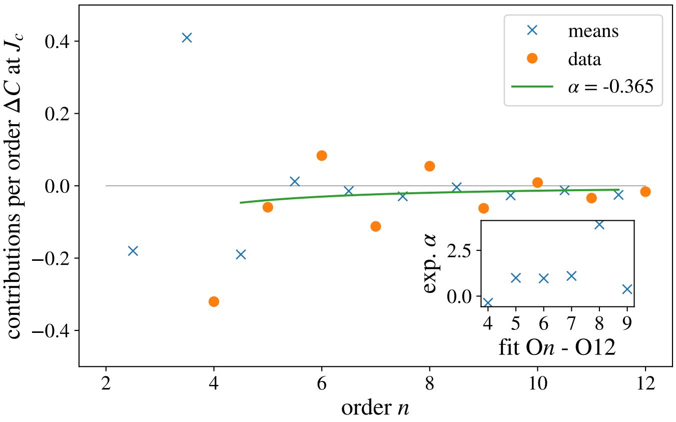

(b) Analysis of the contributions per order by a power law fit.

Figure 4.4: Analysis of the ground-state energy in the frustrated TFIM on the triangular lattice. The inset plot shows the values for α from fit windows from order n to 12. Only the direct fit of a power law gives qualitatively correct values for α. The value $J_c = 0.609$ is used for the critical point.

performed and the inset plots show the results of fits to data from order n to order 12. The resulting exponents seem to be scattered around the correct value, indicated by a horizontal gray line. Still, the scattering prohibits to extract a tendency to better convergence for higher orders. This stems from a surprising feature of the data which is most clearly visible in the finite difference plot. It exhibits a strong even-odd effect which is also present in Markus Pirkes NLCE data, but only very faintly. The series does not display the feature at all. Here, the oscillation has comparable magnitude to the data itself destabilizing the fits. This oscillation can only partly be suppressed by considering means between neighboring orders as depicted by blue crosses, with respect to which all fits have been performed.

For the ferromagnetic TFIM on the square lattice the same analysis is carried out and presented in Fig. 4.3. The difference is that one finds new contributions only at even orders as for the bare series. Hence, only few fit windows can be used reasonably. The quality of the exponents is comparable to those on the triangular lattice.

In Fig. 4.4 the results for the frustrated TFIM on the triangular lattice are shown. Here, also the series shows a strong even-odd effect which Markus Pirke also found for NLCE [35]. The NLCE data does not converge for high orders since the absolute value of the alternating contributions per order diverges. This behavior sets on at couplings considerably lower than the critical point already. The deepCUT data suppresses the alternation as compared to NLCE or the series but not fully. Importantly, the data seems to be convergent and one can apply fitting techniques considering means between neighboring orders. The low and negative value of $\alpha = -0.01526(30)$ of the 3dXY universality class is harder to capture than the 3d Ising value. In addition, the plot of contributions per order cannot be presented as a log-log plot since the magnitude of the oscillation exceeds the magnitude of presumably ideal data introducing sign changes to the contributions. Only the direct fit of the power law gives stable results for α in the order of 1×10^{-3} with a trend towards values of larger magnitude. Even though this is no quantitative estimate of the exponent, it is a valuable result as it captures the feature of the exponent being small and negative. Generally, due to the offset, α is hardly detectable directly rather than using relations to other exponents. It must be mentioned that for the fit another local minimum is found for a small positive value of α.

Overall, the ground-state energies of all models could be analyzed successfully. It has turned out to be most reliable to fit a power law with offset to the bare data as compared to considering finite differences. For the ferromagnetic models both techniques yield consistent results in contrast to a naive fit without offset. This is a strong indication that the offset is the dominant correction to the universal scaling behavior which makes the analysis of the heat capacity notoriously difficult. That this offset can be efficiently suppressed by considering contributions per order is likely due to its physical nature. Assumed to be constant around the critical point, it should be determined by low length scales only, which are captured by low perturbative orders. These are eliminated from the higher data points if finite differences are considered. Looking at the form of the function in Eq. 4.5, one could naively assume that it is sufficient to consider the third derivative instead of the second with the expectation

$$\partial_J^3 E_0 \sim n^{\frac{\alpha-1}{\nu}} \tag{4.6}$$

for the scaling behavior. Taking the derivative with respect to the control parameter rather than the length scale or order has not been successful in suppressing the offset, however. Also, numerical derivatives of third order start to suffer from numerical errors.

4.1.2 Comparision to NLCE results

The NLCE data for the heat capacity used in the Bachelor thesis of Markus Pirke has been made available for this project. Data for the heat capacity in the ferromagnetic single-layer TFIM on triangular lattice is shown in Fig. 4.5. The value for the exponent $\alpha \approx 0.08$ which has been found by fitting a power law [35] could not be reproduced. Here, we show the data in a log-log plot and fit power laws to the data in fit windows from order n to order 15 in analogy to the analysis of deepCUT data. We further leave out the data point for order 16 as it exhibits a strong numerical error. The exponents obtained like that oscillate with a tight amplitude around the literature value for $\alpha/2$ shown by the gray horizontal line in the inset of Fig. 4.5. From order 6 the data for the exponent starts to converge monotonously. The limit of $\alpha/2$ is consistent with the earlier mentioned finding of $\xi \sim n_{\mathrm{NLCE}}^{1/2}$.

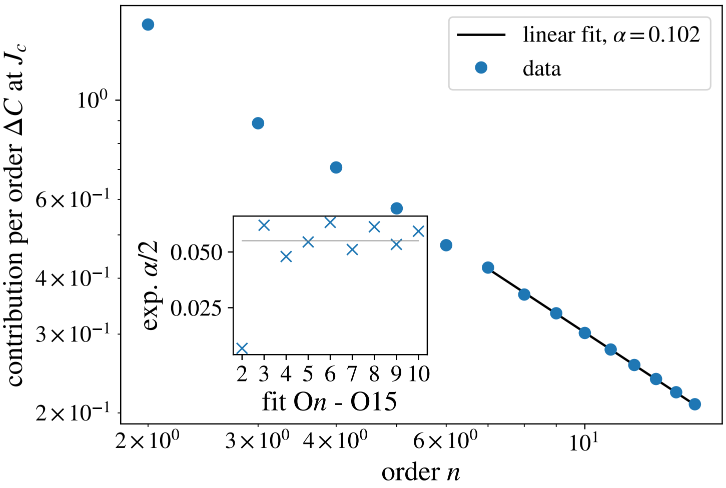

Figure 4.5: Heat capacity of the ferromagnetic TFIM on the triangular lattice at the critical point from NLCE [35]. A power law is fitted to the data from order n to order 15. The resulting exponents are shown in the inset plot and are scattered around the literature value for $\alpha/2$.

4.1.3 Iterative scheme to detect quantum criticality based on the energy gap

The gap is an important quantity for the analysis of quantum criticality since it displays much weaker corrections than the ground-state energy. The expectation for its scaling at the critical point

$$\Delta(J_c) \sim \xi^{-z} \tag{4.7}$$

does usually not give access to information about the universality class, as z is typically independent of the universality for a wide range of models. However, this can in reverse be used to check the scaling of the length scale ξ with respect to the truncation parameter or perturbative order n. DeepCUT data of the energy gap around the critical point is used to fit a power law of Δ against n. The resulting exponents for two fit windows (order 3(4) to order 9(10)) are plotted against the coupling J for the single-layer models in Fig. 4.6. For the ferromagnetic models one finds that the fit windows agree within good accuracy at the critical point on $z = 1$. Even from the fit errors it is apparent that the data is described best by a power law at the critical

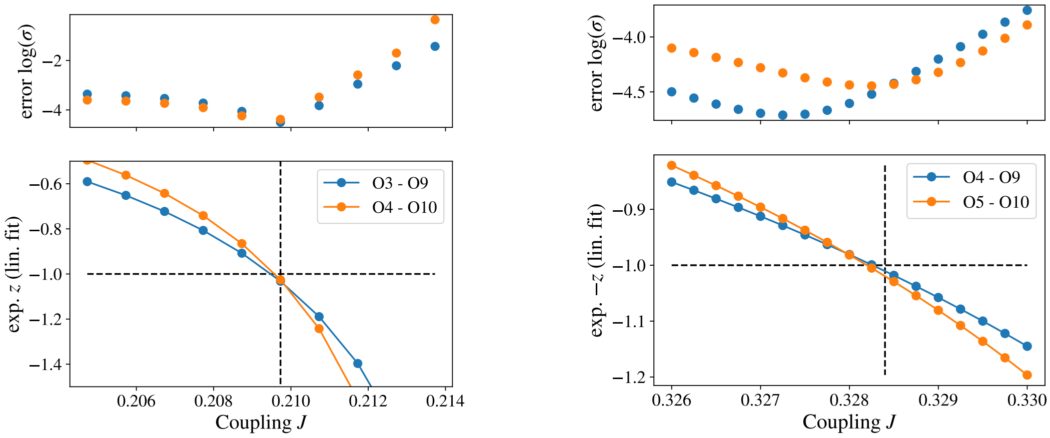

(a) Ferromagnetic TFIM on the triangular lattice.

(b) Ferromagnetic TFIM on the square lattice.

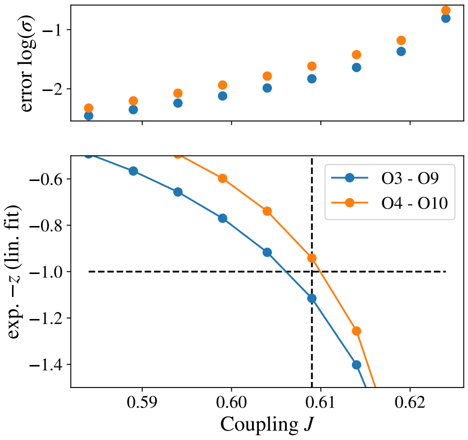

(c) Frustrated TFIM on the triangular lattice.

Figure 4.6: Analysis of the correspondence of the length scale ξ and the perturbative order n. For couplings J in the vicinity of the critical point a linear fit to the logarithm of the energy gap against the logarithm of the order is performed. At the critical point one finds that the fit errors (upper panels) for the well-behaved ferromagnetic models are minimal, implying that here the decay of the gap with order is well-described by a power law. For couplings away from the critical point the slope of the fit changes if the fit window is changed from order $3-9$ to $4-10$, in contrast. For all models at the respective critical point, indicated by a vertical dashed line, the exponent of the power law agrees well with $-1=-z$ pointing towards $\xi \sim n$.

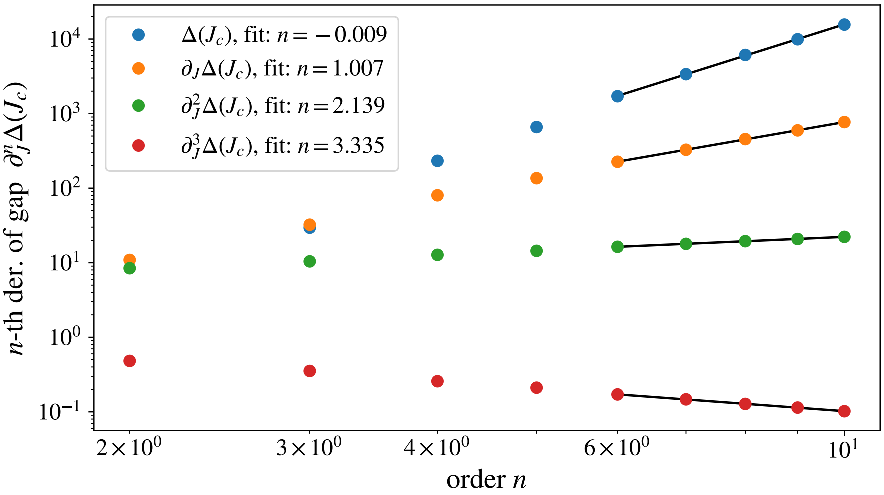

Figure 4.7: Scaling of the gap and the first three derivatives of the gap with length scale. Linear fits to the highest data points reveal values for the underlying exponent $-z+\bar{n}/\nu$ from which we extract the values for $\bar{n}$ are given in the legend. The expectation of $\bar{n}=0,1,2,3$ for the shown derivatives is met up to sufficient accuracy for the arguments made earlier which rely on the scaling of the n-th derivative of the energy gap.

point. This evidence for $\Delta\sim n^{-1}$ is to be compared to $\Delta\sim\xi^{-z}$ and the expectation $z=1$ and implies

$$n\sim\xi \tag{4.8}$$

which may not seem surprising, but the reliability of this result for deepCUT as compared to other methods such as NLCE is one of the most important results of this thesis. For the frustrated TFIM the data is again disturbed by the oscillation of the gap with respect to even and odd orders which affects the fits for the exponent z. Still, $z=1$ is found close to the literature value of the critical point.

In the next section the power law for the closing of the energy gap which has been derived is of great importance. The derivation relies on a Taylor expansion containing all n-th derivatives of the energy gap and their scaling with length scale described by Eq. 2.10. We have numerically stable access up to the derivatives of the energy gap up to third order, which are plotted against the perturbative order for the ferromagnetic TFIM on the triangular lattice in Fig. 4.7. By assuming that the exponent is indeed given by $-z + \bar{n}/\nu$ we can extract values $\bar{n}$ from slopes of the fits if we use literature values for ν and z. We expect $\bar{n} = n$ for the n-th derivative. As expected from the earlier analysis, we find remarkably good agreement for the bare gap. That the agreement is almost equally well for the first derivative which only exhibits a deviation of 1%, is an important insight, since this will allow us to reversely extract ν if we assume $\bar{n} = 1$. For the higher-order derivative the error increases to 7%(11%) for the second (third) derivative. At the same time we realize that generally, the magnitude of the derivatives decreases fast with the order of the derivative. Hence, errors are not expected to impact the expansion in the derivation for the closing of the gap heavily. We will later also find further numerical evidence that the result of the derivation holds for deepCUT data.

The correspondence of perturbative order and length scale in Eq. 4.8 is first of all important to justify the analysis of the heat capacity in the previous section. Furthermore, it serves as the starting point to analyze quantum criticality based on the energy gap. We have derived the relations

$$\partial_J \Delta(J_c) \sim n^{-z+\frac{1}{\nu}}, \tag{4.9}$$

$$J_0 \sim n^{-\frac{1}{\nu}} \tag{4.10}$$

for the first derivative and the closing of the gap denoted by J_0, where order and length scale can be exchanged. The first relation can be used to extract ν if $z = 1$ is either known or extracted from an analysis as above, and if, more importantly, the critical point J_c is known. At the beginning of the chapter it has been pointed out that the naive way of extrapolating the critical point from a linear fit to the closing of the gap against the inverse order is not sufficient as could be seen in Fig. 4.1. In doing so, implicitly an assumption about the second scaling relation in Eq. 4.9 is made, namely $\nu = 1$. For this error can be corrected by plotting the data against $n^{-1/\nu}$ as done in Fig. 4.8a using the literature value for ν for the frustrated TFIM. The resulting extrapolated critical point $J_c/h = 0.609$ has a much weaker dependence on the fit window and is well within the errors of the Monte-Carlo literature value of $0.610(4)$ [30]. For the ferromagnetic models shown in Figs. 4.8c and 4.8e agree well with the results from Hamer [15]. In contrast to the frustrated TFIM, the scaling behavior is nearly perfect if the lowest orders

Table 4.1: Iterations for the frustrated TFIM on the triangular lattice. Literature values are $\nu = 0.672$ [38] and $J_\mathrm{c} = 0.610(4)$ [30]

Iteration	ν	J_c
1	1	0.5922
2	0.707	0.6070
3	0.687	0.6080
4	0.687	0.6080

are neglected, giving numerical evidence for the derived scaling relation for the closing of the gap.

The relation for the first derivative of the energy gap is applied at the right-hand side of Fig. 4.8. The literature values for the critical points are used. The values of ν for the frustrated TFIM can be well distinguished from the values for the ferromagnetic models. This underlines the usefulness of the scaling-based approach to quantum criticality in the context of deepCUT. Fig. 4.8 shows that either the critical point or the critical exponent ν can be found precisely if the corresponding other quantity is known. This motivates an iterative technique: Starting with the estimate $\nu = 1$ one can alternatingly feed the the latest value for J_c (ν) to the fit for ν (J_c). The results for the TFIMs on the triangular lattice and the quadratic lattice are given in Tables 4.1, 4.2 and 4.3. The method converges quickly and gives results for the critical point and the critical exponent at similar precision as dlog-Padès. No literature values apart from $z = 1$ need to be known beforehand. Hence, the universality can be determined with high certainty.

One of the main sources of uncertainty of the scheme is the discretization of the coupling J. For performing the scheme a set of data points $\Delta^{(n)}(J_i)$ is generated for all available orders n at couplings J_i which are chosen equidistantly around the presumed critical point and which are required to cover the closing of the gap in all orders, importantly. From that the closing of the gap $J_0^{(n)}$ can be extracted via linear interpolation, and the first guess for J_c is extrapolated assuming $\nu = 1$ in the first step of the scheme. Then the coupling J_i which is closest to J_c is chosen to fit the first non-trivial value of ν in the second step using the first derivative of the

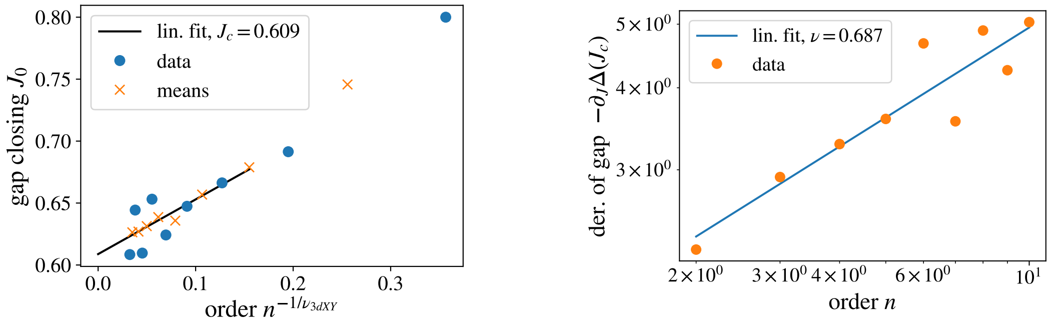

(a) Critical point $J_c = 0.6088$ (lit: 0.610(4) [30]) of the frustrated TFIM.

(b) Critical exponent $\nu = 0.687$ (lit: 0.672) of the frustrated TFIM.

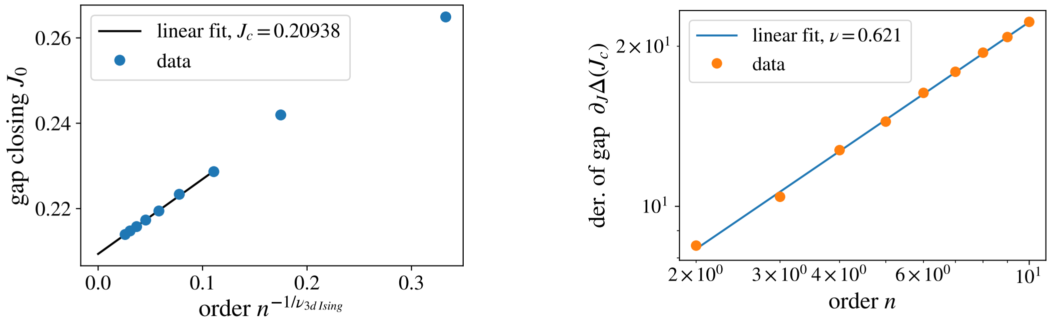

(c) Critical point $J_c = 0.20938$ (lit: 0.20973(2) [15]) of the ferromagnetic TFIM on the triangular lattice.

(d) Critical exponent $\nu = 0.621$ (lit: 0.630) of the ferromagnetic TFIM on the triangular lattice.

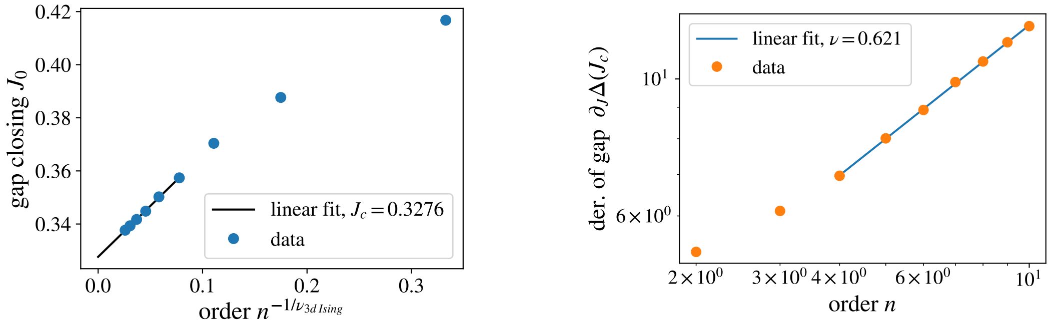

(e) Critical point $J_c = 0.3276$ (lit: 0.32850(10) [15]) of the ferromagnetic TFIM on the square lattice.

(f) Critical exponent $\nu = 0.621$ (lit: 0.630) of the ferromagnetic TFIM on the square lattice.

Figure 4.8: Demonstration of the scaling relations for $\partial_J\Delta$ and J_0. On the left-hand side extrapolations for the critical point based on the closing of the gap, and on the right-hand side fits for the exponents ν to the derivative of the energy gap are shown. Literature values for the critical point and the critical exponent are used. For all models the results agree well with the expectation.

Table 4.2: Iterations for the ferromagnetic TFIM on the triangular lattice. Literature values are $\nu = 0.630$ and $J_c = 0.20972(2)$ [15].

Iteration	ν	J_c
1	1	0.20354
2	0.665	0.20883
3	0.628	0.20940
4	0.621	0.20953
5	0.621	0.20953

Table 4.3: Iterations for the ferromagnetic TFIM on the square lattice. Literature values are $\nu = 0.630$ and $J_c = 0.32850(10)$ [15].

Iteration	ν	J_c
1	1	0.31466
2	0.688	0.32549
3	0.642	0.32710
4	0.635	0.32733
5	0.634	0.32737
6	0.634	0.32737

gap. Eventually in later iterations, the change in the guess for the critical point may be smaller than the spacing of the coupling values δ which will result in the same ν as in the previous step. Hence, the discretization of J_i induces a discretization of the accessible values for ν. The critical point itself is not subject to the discretization δ, but only to the discretization of the ν values for each of which a separate extrapolating fit can be performed to give a value for the critical point. By that, the spacing δ between the values of J_i may limit the precision up to which the ν and the critical point J_c can be extracted. The spacing for the frustrated TFIM is 5×10^{-3}, for the ferromagnetic TFIM on the triangular lattice 1×10^{-3} and on the square lattice 2.5×10^{-4}. The induced discretization on ν is typically in the order of 10^{-3} and the reinduced discretization on the critical point is typically in the order of 10^{-4}. However, these numbers cannot be expected to solely determine the errors on the results. Another source of errors is the numerical derivative which is calculated as a finite difference with $h = \delta$ in all cases. The influence of the choice of h has been checked to be small compared to the overall error of the results.

The last source of uncertainty is the arbitrary choice of fit windows which has the largest influence on the results. For the critical point it has been found to be always beneficial to exclude the lowest orders from the fit as expected. For the exponent however, including all orders has been found to be more reliable for the models on the triangular lattice. In particular for the frustrated model, the choice of the fit window is crucial. Here, we can determine a reasonable choice by comparing to the literature values for J_c and ν. If the lowest order in the fit windows as in Fig. 4.8 are excluded additionally, one finds $J_\mathrm{c} = 0.6099$ and $\nu = 0.707$ for the frustrated TFIM, for example. This suggests errors in the order of 10^{-2} for the exponent and 10^{-3} for the critical point. These errors are more severe compared to those from the discretization and are expected to be the limiting errors of the scheme. Later, when we apply the scheme to the frustrated TFIM bilayer, the fit windows of the frustrated single-layer TFIM from Fig. 4.8 are adapted since qualitatively similar results are expected. How a proper choice for new models can be made in general must still be clarified.

4.1.4 Further analysis of the energy gap

Even though the iterative scheme has been found to be most successful in revealing quantum criticality based on deepCUT data, other possible ways of analysis have been investigated. First, a method introduced by Kris Cöster [39] is applied which aims to combine the non-perturbative character of the data with the strength of dlog-Padé extrapolants. It uses data for the energy gap $\Delta^{(n)}(J_\mathrm{c})$ where the critical point is assumed to be known. This data is used to construct a series in an artificial parameter λ

$$F(\lambda) = \sum_{m=1}^{n} \left(\Delta^{(m)}(J_\mathrm{c}) - \Delta^{(m-1)}(J_\mathrm{c}) \right) \lambda^m \tag{4.11}$$

which is expected to have a pole at $\lambda = 1$ with residuum $z\nu$ in analogy to the standard analysis of series expansions of energy gaps. All non-defective

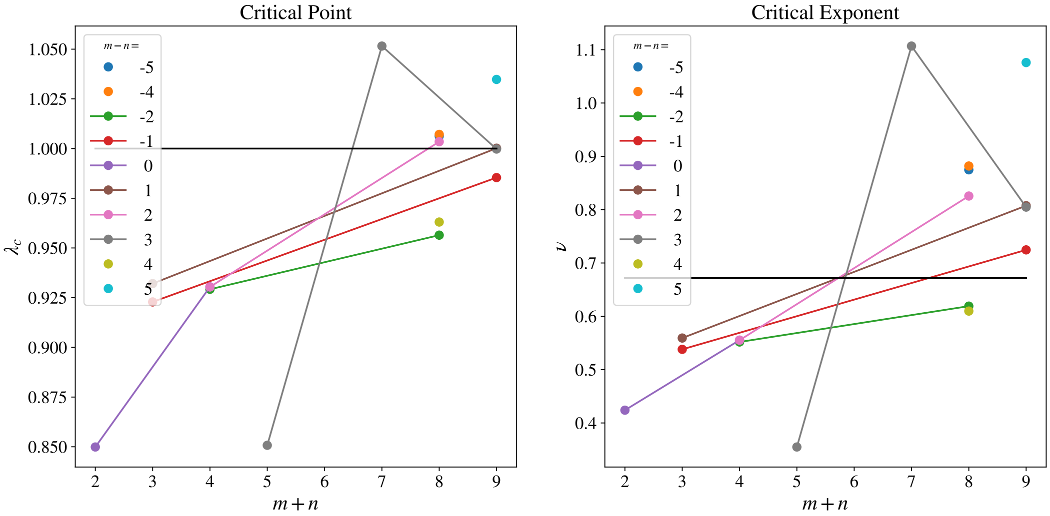

Figure 4.9: Dlog-Padé approximants for the energy gap of the deepCUT data for the frustrated TFIM on the triangular lattice. The approximants $P[m/n]$ are grouped in families with fixed $m-n$. Such families are expected to show a converging trend with higher orders $m+n$. The expected value for ϵ_c, shown on the left-hand side, is unity [39] which is indicated by a vertical line as also the literature value of the critical exponent ν which is shown on the right-hand side.

extrapolants $P[m/n]$ are plotted in families of constant $m-n$ in Fig. 4.9. The expected pole at $\lambda = 1$ is captured well by the higher order approximants. The values for the critical exponent νz are consistent with the literature value indicated by a horizontal line but are not precise enough to be considered predictive.

Another way of accessing the critical exponent has been explored. The underlying idea is not to use deepCUT data at the critical point but in an intermediate regime of the coupling, where deepCUT is still expected to be quantitative. The benefit is that one does not need to rely on scaling relations as for the methods presented earlier. In Figs. 4.10 – 4.12, the quantity

$$(J - J_c)\partial_J \log(\Delta(J)) \tag{4.12}$$

is plotted against $1 - J/J_c$ inspired by the principle of dlog-Padé approximants. At the critical point the gap is expected to behave as $(J - J_c)^{z\nu}$ which implies that the plotted quantity should converge to $z\nu$ at $J = J_c$. The

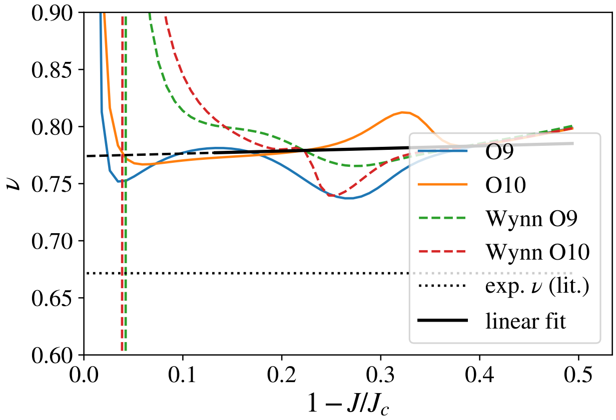

Figure 4.10: Local estimator of the critical exponent ν for the frustrated TFIM on the triangular lattice. DeepCUT results of order 9 and 10 and Wynn extrapolations in the order thereof are shown. All results are averaged between even and odd orders. A linear fit to the average of the Wynn-extrapolated results is used as an extrapolation to the critical point (black dashed line).

critical point is taken to be the literature value. In Fig. 4.10, the results for the frustrated TFIM are shown. The highest order available from deepCUT are shown as means with the respective lower order to suppress the alternating behavior. Additionally, Wynn extrapolations [40] in the perturbative order are considered which stabilize the results to even higher values of the coupling. A linear fit is considered to extrapolate to the critical point. The exponent is way overestimated by the approach.

In Fig. 4.11 a similar analysis of the ferromagnetic model on the triangular lattice and in Fig. 4.12 on the quadratic lattice is shown. No averaging of even and odd orders is necessary here. The exponents are close to the literature value, but the tendency for the triangular lattice does not point towards convergence to the critical point. It seems that the non-perturbative character of deepCUT does not contribute fruitfully since the exponents at low couplings fit the expectation similarly well or even better than the values in the non-perturbative coupling regime. We have also tried to tune the critical point assumed for the method, in order to see convergence to the literature value of the extrapolated exponent. However, this requires critical points which are way below the errors of the literature values.

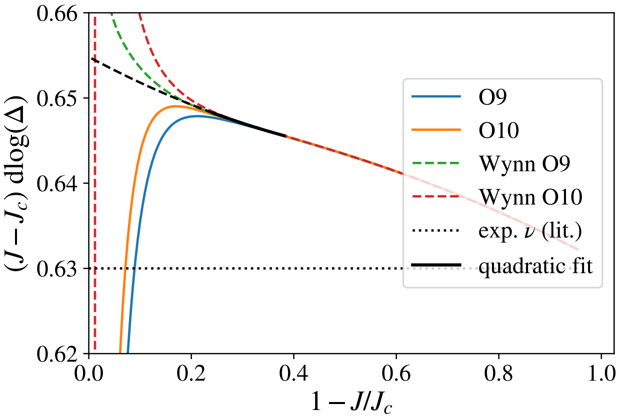

Figure 4.11: Local estimator of the critical exponent ν for the ferromagnetic TFIM on the triangular lattice. DeepCUT results of order 9 and 10 and Wynn extrapolations in the order thereof are shown. A quadratic fit to the average of the Wynn-extrapolated results is used as a extrapolation to the critical point (black dashed line).

4.2 The frustrated TFIM bilayer

4.2.1 Phase diagram and criticality

For the frustrated transverse-field Ising bilayer the energy gap is calculated with the triplonic model and the model in terms of independent hardcore bosons. All results concerning the quantum criticality of the model use the hardcore-bosonic model. In order to trace out the quantum critical line of the model, the energy gap is calculated for various configurations of the dimer parameters for the symmetric case $h := h_1 = h_2$

$$(J_\perp, h) \in \left\{ \left(\sin\left(\frac{j}{10}\frac{\pi}{2}\right), \cos\left(\frac{j}{10}\frac{\pi}{2}\right) \right), j = 0, \ldots, 10 \right\}. \tag{4.13}$$

Remarkably, the results for $j = 0$ shown in Fig. 4.13a do not coincide with the frustrated single-layer TFIM. For consistency with the earlier results, we use the single-layer model for the results in that limit. The energy gap at all parameter settings is available up to order 7. As always for the energy gap, the $1 : n$-generator is used. In contrast to the single-layer models we find

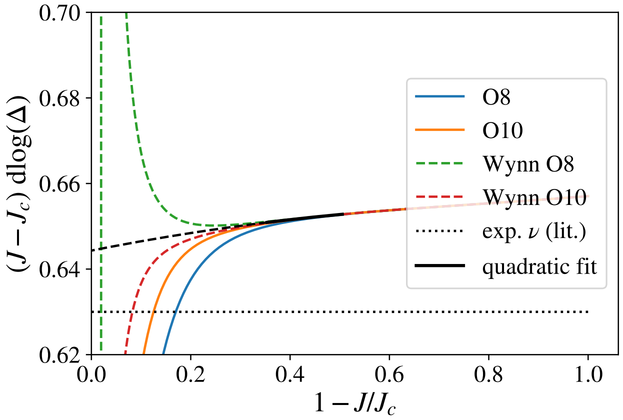

Figure 4.12: Local estimator of the critical exponent ν for the ferromagnetic TFIM on the quadratic lattice. DeepCUT results of order 8 and 10 and Wynn extrapolations in the order thereof are shown. A quadratic fit to the average of the Wynn-extrapolated results is used as a extrapolation to the critical point (black dashed line).

divergences in the data. They appear for $j \in \{0,1,8,9,10\}$. In the limit of weak coupling for $j = 0,1$ shown in Figs. 4.13a and 4.13b the energy gap of order 6 does not converge to the point where it presumably would close. Order 7 does not exhibit this problem which may be caused by the fact that it closes later due to the alternating behavior. In the limit of strongly coupled layers, the energy scales of the model are split into low energy physics in the earlier introduced pseudospin degree of freedom and a large energy scale, which causes severe divergences in that limit as can be seen for $j = 9$, shown in Fig. 4.13f and $j = 10$ where no useful data is obtained and no analysis is carried out. Surprisingly, for $j = 8$ the gap diverges in order 7 only in an intermediate regime and the closing of the gap is captured again, as can be seen in Fig. 4.13d. For all $j \in \{1,\ldots,8\}$ gaps in the data are filled by fitting a degree 15 polynomial to the 16 last data points which converged. The fits are represented by dotted lines. The result has been found to be robust against the changes in the order of the polynomial and the choice of which data points are used for the fit.

The iterative scheme presented earlier is applied to all analyzable cases. The extrapolation of the critical point has been fitted to means of even and odd

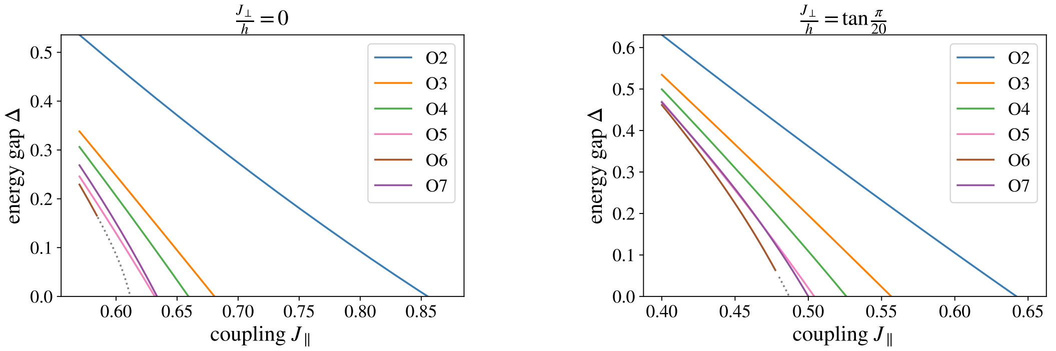

(a) Divergence in order 6 for $j = 0$. This data is replaced by the single-layer data for the analysis.

(b) Divergence in order 6 for $j = 1$. The data point may be influenced by the extrapolation.

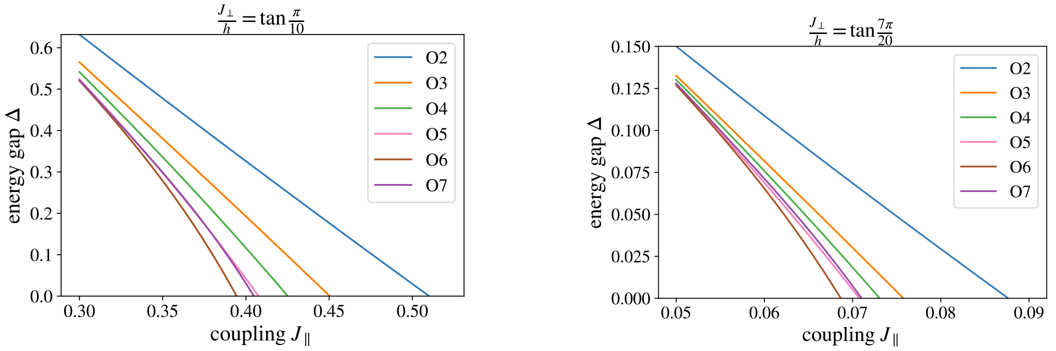

(c) For $j = 2$ we find the first set of parameters without divergences before the gaps close.

(d) For $j = 7$ we find the last convergent set of parameters.

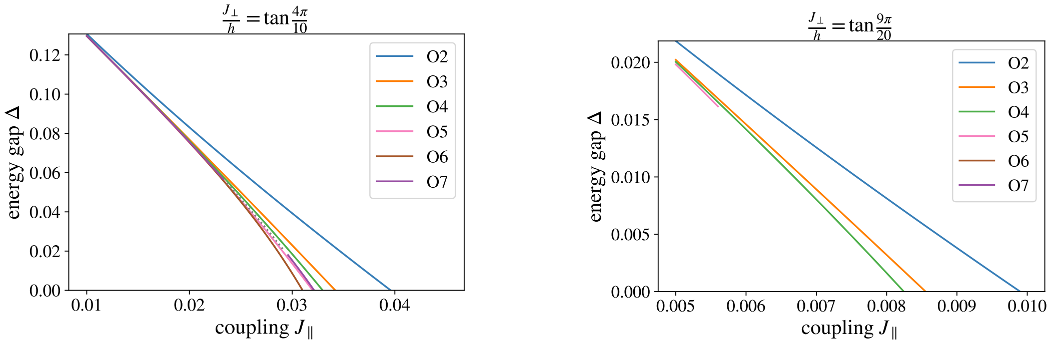

(e) An intermediate divergence in order 7 is found for $j = 8$.

(f) Severe divergences starting from order 5 for $j = 9$. The data is not analyzed.

Figure 4.13: DeepCUT data of the energy gap for the frustrated transverse-field Ising bilayer. The intra-layer coupling is chosen as $J_\perp/h = \tan\left(\frac{j}{10}\frac{\pi}{2}\right)$ for $0 \leq j \leq 10$. Gray dashed lines indicate reconstructed data in regions where deepCUT diverges.

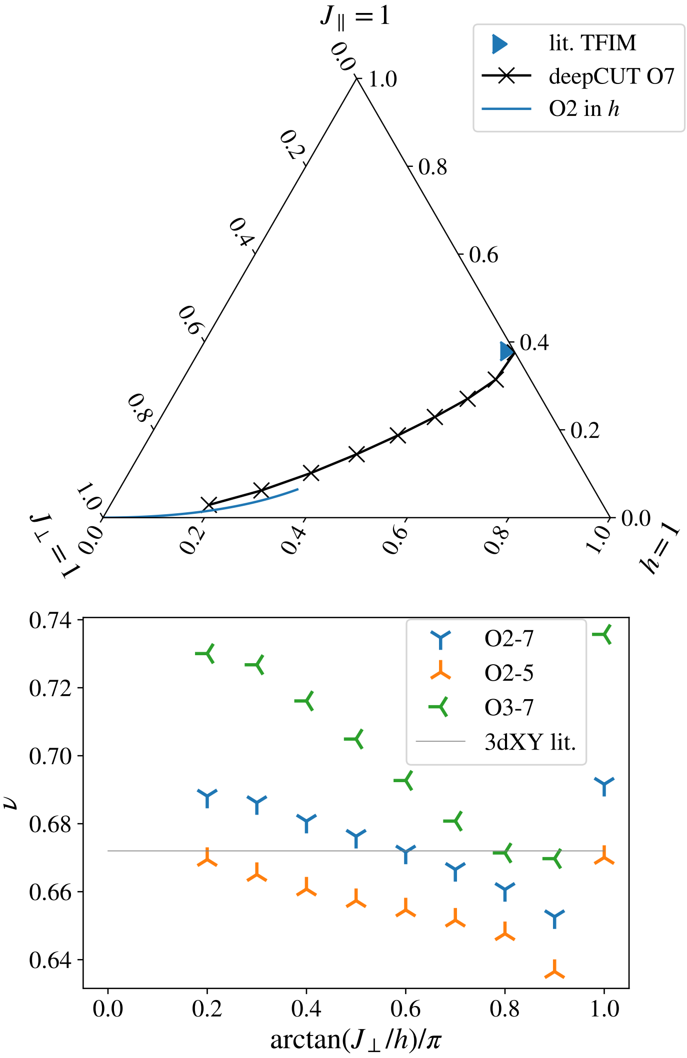

Figure 4.14: Phase diagram and critical exponents of the frustrated transverse-field Ising bilayer. The phase diagram is a cut through the parameter space along the surface $J_\parallel + J_\perp + h = 1$. The right-hand side is the limit of decoupled layers, for which the numerically well known phase transition is indicated by the blue triangle, and the lower axis is the perturbative limit of decoupled dimers. Black crosses are the results for the critical point calculated with the iterative scheme. The blue line and the dashed blue line are the result for second and third order perturbation theory in the limit $J_\parallel = h = 0$. The exponents corresponding the each of the data points in the phase diagram are shown in the lower panel. Three fit windows are shown to capture the uncertainty on the result. The horizontal line is the literature value for the transition.

orders from order $3, 4$ to $6, 7$ and all orders are considered without averages for the exponent ν. This is in analogy to the analysis of the frustrated single-layer TFIM. For the case of decoupled layers the critical point is 3.8% lower than the literature value. Even though this result is not used but rather the result from the single-layer model which only deviates by 1.1%, it can be considered to suggest an order of magnitude of the error of the critical line.

For the exponent, the uncertainty is analyzed by considering multiple fit windows on the data at the critical point obtained from the iterative scheme applied with the full fit window from order 2 to 7. The data points at order 6 and 7 are the first ones which are strongly impacted by the alternation of orders. Therefore, only the fit windows $2-5$ and $3-7$ are reasonable to extract a trend for higher orders. The data suggests a trend towards higher exponents. However, this may just be due to the onset of alternation. The data points are consistent with a critical line which is in the 3dXY universality class throughout. In particular, no sign of a sudden change in the exponents is visible, which would point towards an intermediate phase on the other side of the critical line which does not exhibit a emergent $O(2)$ symmetry and is therefore not separated by a 3dXY transition.

4.2.2 Analysis of divergences in deepCUT

We consider the triplonic model for the TFIM bilayer as an example for a divergence in the deepCUT flow. In the limit of decoupled layers the 6th order has been found to diverge for values of $J_{\|} \gtrsim 0.59$. We record the dispersion in the case $J_{\|} = 0.608$ throughout the flow until we find the divergence. The resulting dispersions at various values of the flow parameter l are shown in Fig. 4.15 as heat maps. Note that the color map resolves the data differently in all snapshots. Just by considering the range of the color maps, in the third snapshot at around $l \approx 37$ the first dip in the dispersion is found. In the 6th snapshot the minimum of the dispersion shifts to $(0, 0)$ indicating a particle decay into the one-quasi-particle continuum. It stems likely from a combination of two particles from the lower band edge of the two-particle continuum with opposite momentum. The physical minima of the dispersion, which are visible in the first two snapshots, show 6 minima distributed symmetrically around $(0, 0)$. Two of these minima are distinct considering the periodicity of the Brillouin zone. The one-quasi-particle state causing the divergence consists likely of particles with exactly these momenta. Starting from $l \approx 41$ the $(0, 0)$-momentum state first has minimal energy, oscillates to having maximal energy before it drops again to become the minimum. After that the dynamics cause a divergence according to the algorithmic criterio, that the ROD exceeds 1×10^8 times its global minimum, as introduced earlier.

The analysis underlines the assumption that the divergences found in the deepCUT results for the bilayer model are due to energetic overlaps between the different quasi-particle blocks. This is a generic restriction of deepCUT and cannot be avoided. However, that divergent deepCUT data can be easily and successfully expanded by Taylor polynomials, makes that restriction less severe when one seeks to study quantum criticality and the data still converges sufficiently close to the quantum critical point.

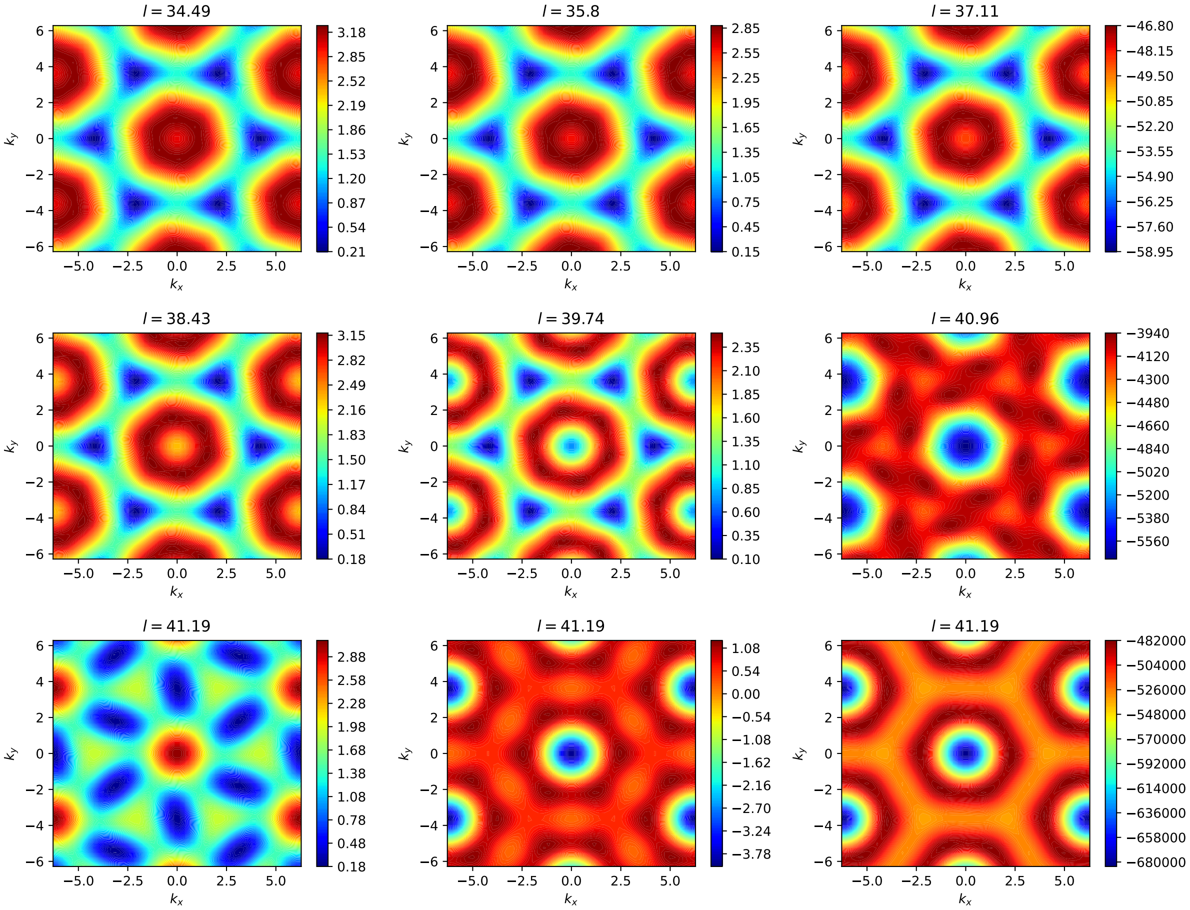

Figure 4.15: Snapshots of the dispersion during the flow of the Hamiltonian for the symmetric bilayer TFIM in the limit of decoupled layers. The intra-layer coupling $J_\perp$ is 0.608 close to the phase transition. The flow parameter l increases from left to right and top to bottom. In the third snapshot at $l \approx 37$ the first signs of the divergence can be seen. The divergence likely stems from a decay of two particles with opposite momentum into the single particle continuum at zero momentum. This manifests in the new minimum of the dispersion at zero momentum in the sixth snapshot at $l \approx 41$.

5 Conclusion

We have implemented the methods epCUT and deepCUT for various TFIMs. The code supports the geometries of the square and triangular lattice and the local algebras of one or two hardcore bosons per site, or three triplonic excitations on each site. That allowed us to study the quantum criticality of a wide range of models which to our knowledge has not been done before using deepCUT.

As a first step, we have considered ferromagnetic and antiferromagnetic single-layer TFIMs on the accessible lattice geometries to develop a method to distinguish between quantum phase transitions in the 3dXY universality class and the 3d Ising universality class. The success of the analysis relies on the strict agreement between the perturbative order, as the quantity controlling the truncation of deepCUT, and the length scale captured by the deepCUT data of that respective order. In the first step, we have demonstrated this correspondence by analyzing the power law governing the behavior of the energy gap at the critical point. Based on this insight, we have achieved the discrimination between the two universality classes using either the ground-state energy or the energy gap. For the ground-state energy we have obtained values for the critical exponent α by using the power law for the heat capacity with respect to the correlation length. For the 3d Ising universality class the values are scattered around the true value and are off up to a factor of two. The value for the 3dXY universality class, which is hardly accessible directly, is not captured quantitatively, but the main features of the exponent, being small and negative, are found in the deepCUT data. From a newly considered power law for the first derivative of the energy gap with respect to the control parameter, the critical exponent ν has been found to be accessible in a better way than it has been proposed in the literature for non-perturbative data for energy gaps. Based on the general expression for the power law of the n-th derivative of the energy gap, a power law for the closing of the gap has been derived. In the quantum critical regime, this has been used to refine the previous extrapolation technique for deepCUT of fitting linear functions to the data versus the inverse order and has given access to values for the critical point in an accuracy competitive with the best data available for the frustrated TFIM on the triangular lattice. In a more general form, the derivation of the scaling behavior serves as a short-cut between elementary power-law scaling of a quantity and the scaling form for it, otherwise used for finite-size scaling, to which our result is equivalent. We have overcome the restriction of our analysis technique that either the critical point or the critical exponent ν must be known beforehand, by introducing an iterative algorithm which alternatingly finds guesses for both until it reaches convergence. We have successfully demonstrated this technique for all previously studied models considered in this thesis.

While the latter findings are all in the field of method development, we have also studied the quantum criticality of a new model in the second part of the project, in order to demonstrate the usefulness of deepCUT in the context of quantum phase transitions. We have introduced the transverse-field Ising bilayer on the triangular lattice. We have analytically derived two points at which a critical line of the 3dXY universality sets in. In between, this critical line has been mapped out by applying the newly introduced iterative scheme. For this, divergences have been cured by polynomial extrapolation of the data for the gap. The critical exponents ν vary along the critical line but are consistent with the 3dXY universality within the expected uncertainty throughout. In particular, there is no sign of a sudden change of the nature of the transition which could have pointed towards a first-order transition otherwise, for example.

The success of deepCUT in the quantum critical regime opens a wide range of possible further applications. The low-field limit of the ferromagnetic Ising model is a hardly extrapolatable limit [16] which could be tackled with deepCUT, leaving room for an improvement in the results. Going to one-dimensional models such as the frustrated Ising ladder with single diagonal couplings in a transverse field, also other types of transitions like a Berezinskii–Kosterlitz–Thouless transition could be analyzed. This would require to adapt the iterative scheme since not the standard second-order power laws are expected anymore. Importantly, one would also like to be capable of quantifying the errors on the critical point and the critical exponents better. This is intricate since the truncation errors and the freedom of the specifics of the fits involved in the iterative scheme all influence this error. In order to get quantitative approximations for other observables than critical exponents in the quantum critical regime, deepCUT in its bare form is not expected to be the right method. The truncation would have to be modified in order to capture longer length scales without requiring the calculation of all commutators necessary for quantum fluctuations in that range. This may be achieved by going from real space to a mixture of real and momentum space. In that sense, this would be a combination of sCUT [22] and CST [20] and an interesting future direction to study new models with flow-equation based methods.

Bibliography

[1] G. H. Wannier, "Antiferromagnetism. the triangular Ising net," Phys. Rev. **79**, 357–364 (1950).

[2] R. M. F. Houtappel, "Order-disorder in hexagonal lattices," Physica **16**, 425–455 (1950).

[3] R. Moessner and S. L. Sondhi, "Ising models of quantum frustration," Phys. Rev. B **63**, 224401 (2001).

[4] S. V. Isakov and R. Moessner, "Interplay of quantum and thermal fluctuations in a frustrated magnet," Phys. Rev. B **68**, 104409 (2003).

[5] M. Powalski, *Quantum paramagnetism in the kagome and triangular transverse field Ising model*, Master thesis, TU Dortmund, 2012.

[6] L. Balents, "Spin liquids in frustrated magnets," Nature **464**, 199–208 (2010).

[7] S. T. Bramwell and M. J. P. Gingras, "Spin ice state in frustrated magnetic pyrochlore materials," Science **294**, 1495–1501 (2001).

[8] A. Kitaev, "Anyons in an exactly solved model and beyond," Annals of Physics **321**, 2–111 (2006).

[9] R. Moessner and S. L. Sondhi, "Ising and dimer models in two and three dimensions," Phys. Rev. B **68**, 054405 (2003).

[10] H. Krull, N. A. Drescher, and G. S. Uhrig, "Enhanced perturbative continuous unitary transformations," Phys. Rev. B **86**, 125113 (2012).

[11] R. Wiedmann, L. Lenke, M. R. Walther, M. Mühlhauser, and K. P. Schmidt, "Quantum critical phase transition between two topologically ordered phases in the Ising toric code bilayer," Phys. Rev. B **102**, 214422 (2020).

[12] L. Schamriß, L. Lenke, M. Mühlhauser, and K. P. Schmidt, "Quantum phase transitions in the K-layer Ising toric code," Phys. Rev. B **105**, 184425 (2022).

[13] G. S. Uhrig and B. Normand, "Magnetic properties of (VO)2p2o7 from frustrated interchain coupling," Phys. Rev. B **58**, R14705–R14708 (1998).

[14] C. Knetter and G. Uhrig, "Perturbation theory by flow equations: dimerized and frustrated $S = 1/2$ chain," The European Physical Journal B - Condensed Matter and Complex Systems **13**, 209–225 (2000).

[15] H. X. He, C. J. Hamer, and J Oitmaa, "High-temperature series expansions for the (2+1)-dimensional Ising model," Journal of Physics A: Mathematical and General **23**, 1775 (1990).

[16] M. Hörmann and K. P. Schmidt, "Projective cluster-additive transformation for quantum lattice models," SciPost Phys. **15**, 097 (2023).

[17] H. Y. Yang and K. P. Schmidt, "Effective models for gapped phases of strongly correlated quantum lattice models," Europhysics Letters **94**, 17004 (2011).

[18] K. Coester, S. Clever, F. Herbst, S. Capponi, and K. P. Schmidt, "A generalized perspective on non-perturbative linked-cluster expansions," Europhysics Letters **110**, 20006 (2015).

[19] A. B. Kallin, K. Hyatt, R. R. P. Singh, and R. G. Melko, "Entanglement at a two-dimensional quantum critical point: a numerical linked-cluster expansion study," Phys. Rev. Lett. **110**, 135702 (2013).

[20] M. Powalski, G. S. Uhrig, and K. P. Schmidt, "Roton minimum as a fingerprint of magnon-Higgs scattering in ordered quantum antiferromagnets," Phys. Rev. Lett. **115**, 207202 (2015).

[21] M. R. Walther, D.-B. Hering, G. S. Uhrig, and K. P. Schmidt, "Continuous similarity transformation for critical phenomena: easy-axis antiferromagnetic xxz model," Phys. Rev. Res. **5**, 013132 (2023).

[22] N. A. Drescher, T. Fischer, and G. S. Uhrig, "Truncation errors in self-similar continuous unitary transformations," The European Physical Journal B **79**, 225–240 (2010).

[23] L. Lenke, A. Schellenberger, and K. P. Schmidt, "Series expansions in closed and open quantum many-body systems with multiple quasiparticle types," Physical Review A **108** (2023).

[24] M. Hafez-Torbati and G. S. Uhrig, "Singlet exciton condensation and bond-order-wave phase in the extended Hubbard model," Phys. Rev. B **96**, 125129 (2017).

[25] M. Hafez Torbati, N. A. Drescher, and G. S. Uhrig, "Dispersive excitations in one-dimensional ionic Hubbard model," Phys. Rev. B **89**, 245126 (2014).

[26] G. Schmiedinghoff, L. Müller, U. Kumar, G. S. Uhrig, and B. Fauseweh, "Three-body bound states in antiferromagnetic spin ladders," Communications Physics **5** (2022).

[27] M. Hafez-Torbati and G. S. Uhrig, "Orientational bond and néel order in the two-dimensional ionic Hubbard model," Phys. Rev. B **93**, 195128 (2016).

[28] S. Sachdev, *Quantum phase transitions*, 2nd edition (Cambridge University Press, 2011).

[29] C. J. Hamer and M. N. Barber, "Finite-lattice methods in quantum Hamiltonian field theory. I. the Ising model," Journal of Physics A: Mathematical and General **14**, 241 (1981).

[30] Y.-C. Wang, Y. Qi, S. Chen, and Z. Y. Meng, "Caution on emergent continuous symmetry: a Monte Carlo investigation of the transverse-field frustrated Ising model on the triangular and honeycomb lattices," Phys. Rev. B **96**, 115160 (2017).

[31] N. A. Drescher, *Variational and perturbative extensions of continuous unitary transformations for low-dimensional spin systems.* PhD thesis, TU Dortmund, 2014.

[32] A. A. Reischl, *Derivation of effective models using self-similar continuous unitary transformations in real space.* PhD thesis, Universität zu Köln, 2006.

[33] T. Fischer, S. Duffe, and G. S. Uhrig, "Adapted continuous unitary transformation to treat systems with quasi-particles of finite lifetime," New Journal of Physics **12**, 033048 (2010).

[34] E. Hairer, G. Wanner, and S. P. Nørsett, *Solving ordinary differential equations I* (Springer, Berlin, 1993).

[35] M. Pirke, *Numerical linked cluster expansions for the transverse field Ising model*, Bachelor thesis, FAU Erlangen-Nürnberg, 2022.

[36] F. Kos, D. Poland, D. Simmons-Duffin, and A. Vichi, "Precision islands in the Ising and $O(N)$ models," Journal of High Energy Physics **2016**, 36 (2016).

[37] J. Rogiers, E. W. Grundke, and D. D. Betts, "The spin model. III. analysis of high temperature series expansions of some thermodynamic quantities in two dimensions," Canadian Journal of Physics **57**, 1719–1730 (1979).

[38] S. M. Chester, W. Landry, J. Liu, D. Poland, D. Simmons-Duffin, N. Su, and A. Vichi, "Carving out OPE space and precise $O(2)$ model critical exponents," Journal of High Energy Physics **142**, 20006 (2020).

[39] K. Cöster and K. P. Schmidt, "Extracting critical exponents for sequences of numerical data via series extrapolation techniques," Phys. Rev. E **94**, 022101 (2016).

[40] C. Brezinski, "Numerical Analysis 2000 Vol. II: Interpolation and extrapolation," Journal of Computational and Applied Mathematics **122**, ix–xi (2000).

Eigenständigkeitserklärung

Hiermit versichere ich, dass ich die vorliegende Masterarbeit selbstständig verfasst habe. Ich versichere, dass ich keine anderen als die angegebenen Quellen benutzt und alle wörtlich oder sinngemäß aus anderen Werken übernommenen Aussagen als solche kenntlich gemacht habe. Des Weiteren versichere ich, dass diese Arbeit weder vollständig noch in wesentlichen Teilen Gegenstand eines anderen Prüfungsverfahren gewesen ist.

Erlangen, 1. Dezember 2023

Lukas Schamriß

Danksagung

An erster Stelle möchte ich meinen Betreuern Kai Phillip Schmidt und Matthias Walther danken. Die Implementierung von deepCUT wäre für mich ohne die Module und die ständige Unterstützung von Matthias Walther und Dag-Björn Hering nicht möglich gewesen. Patrick Adelhardt, Jan Koziol und Max Hörmann bin ich dankbar für hilfreiche Diskussionen, die maßgeblich dazu beigetragen haben, eine Methode zum Auswerten der deepCUT-Ergebnisse zu finden. Matthias Mühlhauser und Markus Pirke danke ich für das Bereitstellen von NLCE-Daten. Für die wunderbare Zeit an der Theo I möchte ich allen Lehrstuhlangehörigen danken. Besonders Viktor Kott und Max Bayer danke ich für die vielen schönen Büromomente, die mir in Erinnerung bleiben werden. Bei Matthias Mühlhauser möchte ich mich für das Trompetespielen bedanken.